

Theory of magnetism due to molecular
orbital degree of freedom and electron
correlation in organic conductors

有機導体における分子軌道自由度と電子相関による
磁性の理論

氏名：川村泰喜

所属：名古屋大学大学院 理学研究科 物質理学専攻
(物理系)

2024年3月

Contents

1	General introduction	4
1.1	Condensed matter physics and electron correlation effect	4
1.2	Organic conductors and their diversity	4
1.3	Compensated ferrimagnetism in (EDO-TTF-I) ₂ ClO ₄	6
1.4	Dirac nodal line system [Ni(dmdt) ₂]	7
1.5	Motivation	10
2	Compensated ferrimagnetism in the organic conductor	12
2.1	Simple model of the compensated ferrimagnetism	12
2.2	Low-energy effective model of (EDO-TTF-I) ₂ ClO ₄	14
2.3	Hartree-Fock approximation (HFA)	17
2.4	Many-variable variational Monte Carlo (mVMC) analysis	20
2.5	Analysis of the DAF state	25
2.6	Summary and discussion	27
3	Fragment-orbital-dependent spin fluctuations	28
3.1	Low-energy effective model and formulation	28
3.2	Numerical result in the case of $U = 0$	37
3.3	Numerical result in the case of $U \neq 0$	46
3.4	Summary and discussion	54
4	Conclusion	57

Abstract

Study of the magnetic order and novel physical phenomena related to it is one of the primary problems of condensed matter physics. Organic conductors are the platform for observing various physical phenomena because of their flexibility in elemental substitution and sensitivity to pressure. In particular, novel physical properties that are considered to be related to magnetic ordering have been observed in organic Dirac nodal line systems and organic conductors with inequivalent dimers, but their mechanisms have not yet been elucidated. In this study, I will therefore conduct a theoretical study to elucidate the novel magnetic properties induced by electron correlation effects in organic conductors. Specifically, I investigate a novel antiferromagnetic order in $(\text{EDO-TTF-I})_2\text{ClO}_4$ and anomalous spin fluctuations in the Dirac nodal line system $[\text{Ni}(\text{dmdt})_2]$.

$(\text{EDO-TTF-I})_2\text{ClO}_4$ is the charge transfer salt which contains two inequivalent dimers in a unit-cell in low T ($T < 190$ K). If the two dimers are magnetized with opposite spins in unit-cell, the energy bands split and the ferrimagnetism appears. However, if the system is commensurately filled, the magnetization becomes zero in the ground state. This magnetic order is called compensated ferrimagnetism, which is expected to be useful for generating spin current. I propose $(\text{EDO-TTF-I})_2\text{ClO}_4$ as a material whose ground state can be compensated ferrimagnetism. The ground state of $(\text{EDO-TTF-I})_2\text{ClO}_4$ is calculated by the Hartree-Fock approximation (HFA) and the many-variable variational Monte Carlo (mVMC) method based on *ab initio* calculations. As a result, compensated ferrimagnetism with giant spin splitting is obtained as a candidate ground state.

On the other hand, a single-component molecular conductor $[\text{Ni}(\text{dmdt})_2]$ is the Dirac nodal line system with the Fermi surface. First, I construct the low-energy effective model using the transfer integrals and Coulomb interaction evaluated by the first-principles calculation. The effective model is described by the fragment orbitals, which are molecular orbitals biased to one side of the molecules. The spin susceptibility is calculated by applying the random phase approximation (RPA) to the low-energy effective model. It is found that the spin fluctuations in this material depend on the fragment orbitals due to the characteristic wave functions and Fermi surface. Especially, it is found that the nontrivial intramolecular antiferromagnetic fluctuations are enhanced in the fragment orbitals located on the left and right sides in low T . The Knight shift and spin-lattice relaxation rate, physical quantities measured by nuclear magnetic resonance (NMR), were calculated and compared with experimental results.

The antiferromagnetic properties appear in both materials and involve molecular orbital degrees of freedom. One is the inequivalent dimers and the other is fragment orbitals. This study shows that electron correlation effects and molecular orbital degrees of freedom confer various magnetic properties on organic conductors. New magnetic properties due to molecular orbital degrees of freedom are expected to be discovered in organic conductors.

1 General introduction

1.1 Condensed matter physics and electron correlation effect

Many interesting phenomena and properties have been observed in the materials around us, such as superconductivity, magnetism, and charge order. Their mechanisms cannot be understood by investigating the materials macroscopically. Physics in the materials is dominated by the particles of the Avogadro numbers, such as electrons and phonons. Therefore, quantum mechanics and statistical mechanics are used to study the phenomena in the materials. In modern physics, the electron correlation effect in the materials is researched actively because it plays important roles in the ordered states and transport phenomena. For example, the short-range Coulomb interaction is important for the magnetic order, while the long-range Coulomb interaction can induce the charge order.

1.2 Organic conductors and their diversity

I focus on the organic conductors because of their diversity: many structures are composed of the same composition, structural transitions occur under pressure, and there is a high degree of freedom in molecular substitution. Organic materials are the insulators or semiconductors in many cases because the respective organic molecules take closed-shell structure and the transfer integrals between the molecules are smaller than HOMO-LUMO gap as shown in Fig. 1 (a). Here, HOMO is the occupied molecular orbital with the highest energy eigenvalue (highest occupied molecular orbital), while LUMO is the unoccupied molecular orbital with the lowest energy eigenvalue (lowest unoccupied molecular orbital). They are also called “frontier orbitals”. However, some organic materials have conductivity. They are called “organic conductors”. There are two types of organic conductors “charge transfer salt” and “single-component molecular conductor”. The former acquires conductivity because anions supply carriers despite the large HOMO-LUMO gap ($\sim 1\text{eV}$). Meanwhile, in the latter, the HOMO and LUMO bands are overlapped by the transfer integrals because the HOMO-LUMO gap is narrow ($\sim 0.1\text{eV}$). In this research, (EDO-TTF-I)₂ClO₄ corresponds to the charge transfer salt and [Ni(dmdt)₂] corresponds to the single-molecular conductor. In the organic conductors, fascinating properties and anomalous behaviors are observed. They are governed by the crystal structure, characters of wave functions, and electron correlation effect. I introduce the two intriguing systems next sections. One is the

inequivalent dimer system (Fig. 1 (b)) and the other is the Dirac electron system (Fig. 1 (c)), which has been researched for a long time.

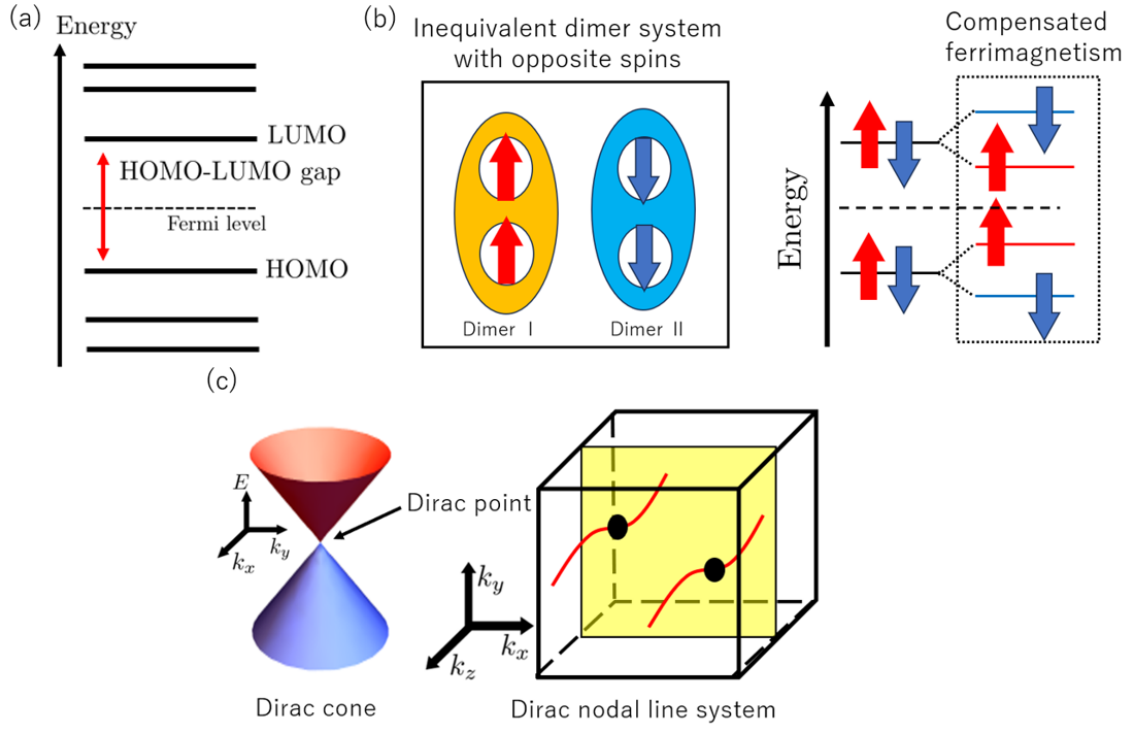


Figure 1: (a) Relationship between HOMO and LUMO. (b) Schematic of the compensated ferrimagnetism in the inequivalent dimer system. (c) Linear dispersion in the Dirac electron system and Dirac nodal lines in the momentum space. Dirac nodal lines are drawn by Dirac points connecting.

1.3 Compensated ferrimagnetism in (EDO-TTF-I)₂ClO₄

Collinear antiferromagnetism has been recognized as conventional magnetism without anomalous phenomena e.g., spin current generation. However, recently, exotic collinear antiferromagnetism with time-reversal symmetry breaking has been discovered, especially altermagnetism [1, 2, 3] and compensated ferrimagnetism [4]. Spin splitting phenomenon appears in these magnetic states nevertheless net magnetization vanishes. These anomalous antiferromagnetisms are the center of attention because spin splitting can induce spin-dependent unique transport phenomena and unconventional superconductivity.

Several materials have been suggested as candidates for materials where altermagnetism is observed [3, 5, 6, 7, 8, 9, 10, 11]. For example, in κ -ET salt [6] and transition metal oxide RuO₂ [8, 10, 12], altermagnetic state with anisotropic spin splitting appears. It is expected that these materials exhibit spin-dependent transport and anomalous Hall effects caused by anisotropic spin splitting. Meanwhile, compensated ferrimagnets exhibit isotropic spin splitting, which makes spin-current generation efficient. The magnetic structure of the compensated ferrimagnet is like a usual antiferromagnet, however, the spin splitting occurs in the energy eigenvalues. Thus, exotic transport phenomena are expected such as spin current. Since van Leuken and de Groot suggest the idea of compensated ferrimagnetic metal (antiferromagnetic half-metal) [13], some candidate materials have been proposed by *ab initio* calculations [14, 15]. Recently, MnF₂ monolayer was suggested as the material where an insulating compensated ferrimagnetism realizes [16]. The compensation condition is robust against small perturbations because the net magnetization of compensated ferrimagnetic insulator is zero due to the Luttinger's theorem [4]. Moreover, crystal symmetry of the compensated ferrimagnets is lower than that of altermagnets [4]. Thus, compensated ferrimagnets are more useful for applications, such as thin-film synthesis, than altermagnets. Nevertheless, only a few compensated ferrimagnets have been found in experiments [17, 18, 19, 20]. The method to realize the compensated ferrimagnets is necessary to make use of them.

I find that the compensated ferrimagnetism can be realized in the organic conductor which has the inequivalent dimers with the opposite spins. Schematics of two inequivalent dimers with opposite magnetization and energy levels of the compensated ferrimagnet are shown in Fig. 1 (b). I propose the organic conductor (EDO-TTF-I)₂ClO₄ as a material where such magnetism appears. It is the pseudo-two-dimensional organic conductor which consists of the EDO-TTF-I with +1/2 charge (3/4 filling) and anion ClO₄ layers, which is shown in Fig. 2 (a) and (b). In $T \gtrsim 190\text{K}$, two EDO-TTF-I molecules belong to one unit-cell, and space-inversion symmetry is macroscopically protected because anions ClO₄ randomly orientate.

Experimentally, insulating electrical resistivity is observed then[21]. In addition, there are two energy bands of which 3/4 is filled near the Fermi level (E_F) and a dimerization gap opens between them. This implies that the system is effectively half-filled. Thus, $(\text{EDO-TTF-I})_2\text{ClO}_4$ is the dimer Mott insulator in $T \gtrsim 190\text{K}$. However, the resistivity measurement and X-ray analysis experimentally show that a phase transition from Mott insulator to semimetal with structural transition occurs at $T \sim 190\text{K}$ upon cooling. It is due to the regular orientation of anions ClO_4 , which is called anion ordering. In this material, anion ordering is the mechanism by which inequivalent dimers are formed. After a structural transition, the unit cell doubles in size; one unit cell contains four molecules (A, A', B, B'). The A and A' (B and B') molecules in the unit cell form a single dimer, which I call “dimer I (dimer II)”. That is not the only phase transition phenomenon observed in this material. The phase transition from semimetal to insulator is observed again at $T \sim 95\text{K}$ with cooling. In contrast to the phase transition at $T \sim 190\text{K}$, it is without a structural distortion.[21] In addition, the magnetic susceptibility monotonically decreases after the metal-insulator transition at $T \lesssim 95\text{K}$ with cooling [21]. In this study, I show that $(\text{EDO-TTF-I})_2\text{ClO}_4$ is the compensated ferrimagnetic insulator in the low-temperature phase.

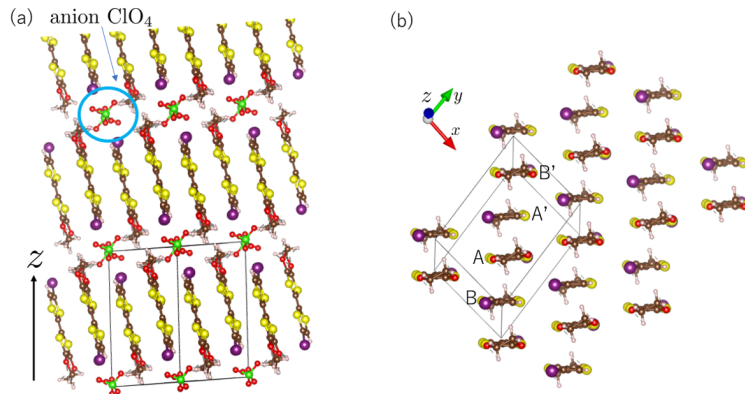


Figure 2: (a) Crystal structure of $(\text{EDO-TTF-I})_2\text{ClO}_4$ along to the stacking direction. (b) Main conduction plane. The black frames represent the unit cell.

1.4 Dirac nodal line system $[\text{Ni}(\text{dmdt})_2]$

I introduce the Dirac electron system and Dirac nodal line system in this subsection. The Dirac electron system has a linear dispersion near the Fermi level because the effective Hamiltonian is equivalent to the massless Dirac equation. The band-crossed point is called the Dirac point. The anomalous transport phenomena are observed in the Dirac electron system.

The resistivity is almost independent of temperature, while the Hall coefficient increases with decreasing temperature. In addition, because of the characteristic wave function, edge-localized electronic states (edge states) are observed.

Dirac electron systems in materials fascinate a lot of researchers due to not only their quantum transport phenomena [22, 23, 24, 25] and large diamagnetism, [26, 27] but also their anomalous behaviors which result from the electron correlation effect.[28, 29, 30, 31, 32, 33] Dirac electron systems in molecular conductors, for example, α -(BEDT-TTF)₂I₃, offer appropriate platforms to research the electron correlation effect because the bandwidth W is much smaller than the onsite Coulomb interaction U ($U/W \gg 1$). [34, 35, 36, 37, 38, 39, 40] α -(BEDT-TTF)₂I₃ is a massless Dirac electron system at high pressure ($P \gtrsim 1.5\text{GPa}$), while a charge order is induced by the long-range Coulomb repulsion in low pressure, [41, 42, 43] where anomalous spin-charge separation on spin gaps [44, 45] and transport phenomena are observed.[46, 47, 48] Moreover, the long-range Coulomb repulsion makes the Dirac cones sharp, which is caused by a logarithmic velocity renormalization. The reshaping of the Dirac cones induces a rare magnetic response.[49, 50, 51] In addition, ferrimagnetism and spin-triplet excitonic fluctuations are observed.[52, 53]

The Dirac electron system in α -(BEDT-TTF)₂I₃ is treated as pseudo-two-dimensional system[40] because it is a stacked molecular conductor and the transfer between different conduction layers is incoherent. On the other hand, if the electron hopping perpendicular to the main conducting layer is coherent, the Dirac points connect and draw lines (rings) in the three-dimensional momentum space, which are called the Dirac nodal lines (rings). [54, 55, 56, 57] Dirac nodal line system can have the Fermi surface and the nodal lines wind due to the dispersion in the stacking direction as shown in Fig. 1 (c). Dirac nodal line (ring) systems have been found in graphite, [58] transition-metal monophosphates,[59] Cu₃N,[60] antiperovskites,[61] perovskite iridates,[62] and hexagonal pnictides with the composition CaAgX (X = P, As),[63] as well as in the single-component molecular conductors [Pd(dddt)₂], [64, 65, 66, 67, 68, 69, 70, 71] [Pt(dmdt)₂],[72, 73, 74, 75, 76] and [Ni(dmdt)₂].[75, 76] In the Dirac nodal line system, not only the phenomena are in common with two-dimensional Dirac electron systems, *e.g.*, the in-plane conductivity[72], but also the characteristic electronic properties such as non-dispersive Landau levels,[77] Kondo effect,[78] quasi-topological electromagnetic responses,[79] and edge magnetism[75] exhibited due to the three-dimensionality. However, the electron correlation effects in the Dirac nodal line systems with Fermi surface have not been investigated in detail.

I focus on the Dirac nodal line system [Ni(dmdt)₂], which is a single-component molecular conductor composed of the Ni(dmdt)₂ molecules. The crystal structure of [Ni(dmdt)₂] is triclinic (Fig. 3) and has space-inversion symmetry. One Ni(dmdt)₂ molecule sits on one unit-cell. The

electronic and magnetic properties of $[M(\text{dmdt})_2]$ ($M=\text{Pt}, \text{Ni}$) were previously investigated by using density functional theory (DFT), and tight-binding models were constructed based on the extended Hückel method and DFT.[72, 73, 74, 75] These researches show that $[M(\text{dmdt})_2]$ is a Dirac nodal line system. Furthermore, electronic resistivity measurements were performed by the conventional four-probe methods. As a result, it is shown that the resistivity of $[M(\text{dmdt})_2]$ is constant to the temperature (T). It is consistent with the behavior in the Dirac electron system[72] and called universal conductivity.[80] In addition, I previously proposed that the nesting between the Fermi arcs localized at the edge and the short-range Coulomb repulsion induce a helical spin density wave (helical edge SDW).[75]

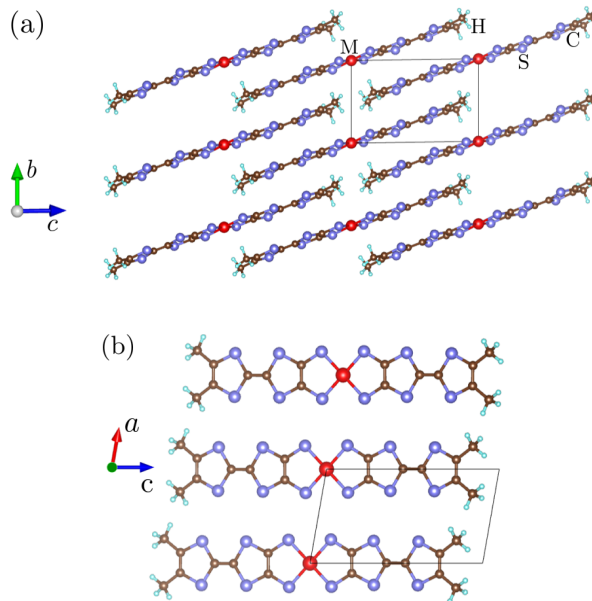


Figure 3: (a) Crystal structure in the b - c plane of $[\text{Ni}(\text{dmdt})_2]$. (b) Crystal structure along to the b -axis. The red, blue, brown, and cyan balls illustrate Ni, S, C, and H atoms, respectively. The black frames indicate the unit cell.

Recently, Knight shift and spin-lattice relaxation rate $1/T_1T$ of $[\text{Ni}(\text{dmdt})_2]$ were observed in a ^{13}C nuclear magnetic resonance (^{13}C -NMR) experiment.[81, 82] $1/T_1T$ decreases with cooling and is almost proportional to T^2 in high T . However, at a low T , it starts to increase with cooling and a peak appears at approximately 30 K. On the other hand, the Knight shift is almost proportional to temperature due to the linear energy dispersion and does not increase with cooling. The mechanism of this anomalous behaviors of the spin fluctuations has not been uncovered.

To solve the problem, I introduce the “fragment orbitals” which are relatively new descriptions for the molecular orbitals, and theoretically research the electron correlation effect on them. The low energy effective

model of single-component molecular conductors, *e.g.*, $[M(\text{tmdt})_2]$ ($M = \text{Ni, Au, Cu}$)[83, 84] and $[M(\text{dmdt})_2]$ ($M = \text{Pt, Ni}$)[74, 75], are described by multiple molecular orbitals localized in a part of the molecule. These molecular orbitals are the energy eigenstates obtained using first-principles calculations and are called “fragment orbitals”[83, 84]. The fragment orbitals are transformed into HOMO and LUMO by a high-symmetry unitary transform. Seo et al. introduce a Hubbard model of $[M(\text{tmdt})_2]$ ($M = \text{Ni, Au, Cu}$), which is described by the fragment orbitals, based on the first-principles calculation.[83, 84] The model which they used is similar to that in this research. They calculated the charge and spin densities by mean-field approximation to investigate the ordered state realized in $[M(\text{tmdt})_2]$. By contrast, I study the spin fluctuations by calculating the spin susceptibility using RPA. I further explain that the fragment orbital concept is a useful way to study the magnetic properties of Dirac nodal line systems in single-component molecular conductors. In addition, models of some charge-transfer salts such as $(\text{TTM-TTP})\text{I}_3$ were also previously constructed by Tsuchiizu et al.[85, 86]

By studying electron correlation effects on fragment orbitals, I find two types of spin fluctuations that depend on the fragment orbitals. Their temperature dependencies are different. One is intramolecular antiferromagnetic fluctuation, which is enhanced at low T . The other is incommensurate spin fluctuation, which increases slowly at high T .

1.5 Motivation

Many electronic states have been discovered and investigated in the long history of condensed matter physics, for example, Mott insulator, superconductivity, Dirac electron system, and so on. These are dominated by the electron correlation effect, characters of the wavefunctions, and the crystal structure. The new ordered states and bound states can be discovered in the system where the electronic correlation effect is important by the chemical pressure and element substitution. I predict that the materials used in this research become the platform where diverse physical phenomena are observed because the organic materials are flexible to the element and molecule substitution.

Research of the magnetic orders and phenomena related to them is one of the important problems in condensed matter physics. I investigate the novel magnetism induced by the electron correlation effect in the organic conductors.

I study the spin fluctuations and magnetic order induced by the electron correlation effect in the organic conductors by the perturbation theory and mVMC method[87, 88]. It has been considered that the spin fluctuations are not enhanced in the Dirac electron system because the DOS near the Fermi energy is low. However, in the research about $[\text{Ni}(\text{dmdt})_2]$, I find that the antiferromagnetic spin fluctuations are enhanced within the

respective molecules by the characteristic wavefunctions in the Dirac electron system and the scattering process in RPA. It is also found that the intramolecular antiferromagnetic spin fluctuations can't be observed by the Knight shift but appear as the upturn in the $1/T_1T$. Moreover, I find that the inequivalent dimers with opposite spins induce a spin splitting phenomenon. It corresponds to the compensated ferrimagnetism. I propose the organic conductor $(\text{EDO-TTF-I})_2\text{ClO}_4$ as the material in which the compensated ferrimagnetic order appears. They are the researches about the antiferromagnetism within unit-cell caused by the molecular orbital degree of freedom. I predict that these studies provide new knowledge about the antiferromagnetism and electron correlation effect in the organic conductors.

2 Compensated ferrimagnetism in the organic conductor

Abstract

Recently, exotic collinear antiferromagnetism with time-reversal symmetry breaking, such as altermagnetism and compensated ferrimagnetism, have been studied extensively for magnetic order. These exhibit spin-splitting phenomena even when the net magnetization is zero, causing anomalous transport phenomena such as spin currents. Anisotropic spin splitting phenomena appear in altermagnets. On the other hand, compensated ferrimagnets exhibit isotropic spin splitting. However, the mechanism to induce the compensated ferrimagnetic state is limited. Therefore, I show how to realize a fully compensated ferrimagnet that exhibits isotropic spin splitting using an inequivalent dimer system in organic conductors. I also find that this magnetism appears in a recently discovered organic conductor (EDO-TTF-I)₂ClO₄ based on *ab initio* calculations. These findings provide a new guideline for realizing fully compensated ferrimagnets with giant spin splitting by using the molecular orbital degrees of freedom of organic materials.

2.1 Simple model of the compensated ferrimagnetism

I propose a path to fully compensated ferrimagnets with giant spin splitting using conventional dimer systems in organic materials. Using a simple one-dimensional model, I introduce that collinear antiferromagnetism with inequivalent dimers causes fully compensated ferrimagnetism. Furthermore, I find that the organic material (EDO-TTF-I)₂ClO₄ [21], which was recently discovered, can realize this magnetism based on *ab initio* calculations. According to the experiments, a structural transition with unit-cell doubling occurs with anion ordering at 190 K in this material. As a result, two inequivalent dimers belong to the unit-cell in $T < 190$ K. In this study, I introduce and solve the low-energy effective Hamiltonian based on the first-principles calculation in $T < 190$ K. I find that the ground state is a collinear antiferromagnetic state with isotropic spin splitting, i.e., a fully compensated ferrimagnet.

At first, to show the important idea for realizing the compensated ferrimagnets, I use a one-dimensional model with a unit cell including two inequivalent dimers. This one-dimensional model is schematically depicted in Fig. 4 (a). The dimer inequivalence is expressed by the intra-dimer transfer

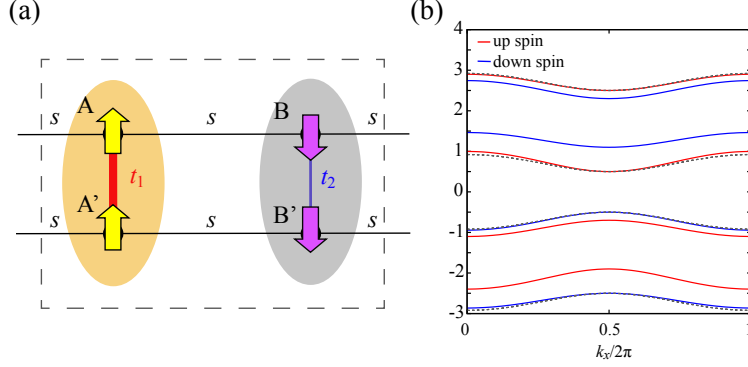


Figure 4: (a) Hopping network of the simple model exhibiting the compensated ferrimagnetism. The unit-cell is represented by the broken frame. (b) Energy band structure obtained by the simple model Eq. 2. That of the equivalent dimer case is shown by the broken lines.

integrals t_1 and t_2 ($t_1 \neq t_2$) and site potential δ . I also assume the collinear dimer antiferromagnetic (DAF) order where the electrons with up(down) spin are located on A and A' (B and B'). This DAF order is not invariant to any combination of time reversal with translation/rotation operations due to inequivalent dimers. Thus, it is predicted that the isotropic spin splitting phenomenon is induced under the DAF order.

In order to investigate the cause of spin splitting in the one-dimensional model, the tight-binding model of the DAF state is expressed by the following Hamiltonian :

$$\mathcal{H} = \sum_{k,\sigma} \mathbf{c}_{k\sigma}^\dagger H_\sigma(k) \mathbf{c}_{k\sigma}, \quad (1)$$

$$H_\sigma(k) = \begin{pmatrix} \sigma\Delta & t_1 & A(k) & 0 \\ t_1 & \sigma\Delta & 0 & A(k) \\ A(k)^* & 0 & -\sigma\Delta + \delta & t_2 \\ 0 & A(k)^* & t_2 & -\sigma\Delta + \delta \end{pmatrix}, \quad (2)$$

where $\mathbf{c}_{\mathbf{k}}^\dagger = (c_{Ak}^\dagger, c_{A'k}^\dagger, c_{Bk}^\dagger, c_{B'k}^\dagger)$, $A(k) = s(1 + e^{-ik})$, and Δ is the order parameter describing the DAF state. σ is the spin index taking +1 and -1 for the up and down spins, respectively. By diagonalizing the Hamiltonian Eq. 2, the following eigenvalues are obtained.

$$E_{0,\sigma,\pm}(k_x) = \delta/2 + t_\pm \pm [(\sigma\Delta + t_- - \delta/2)^2 + 2s^2F(k)]^{1/2}, \quad (3)$$

$$E_{1,\sigma,\pm}(k_x) = \delta/2 - t_\pm \pm [(\sigma\Delta - t_- - \delta/2)^2 + 2s^2F(k)]^{1/2}, \quad (4)$$

where $t_\pm = (t_1 \pm t_2)/2$ and $F(k) = 1 + \cos k$. Thus, it is found that the parameters $t_- = (t_1 - t_2)/2$ and δ , which express dimer inequivalence, cause spin splitting. Furthermore, not only the site potential but also the

difference between two intra-dimer transfer integrals can open an energy gap. Because t_- and δ are constant in momentum space, isotropic spin splitting occurs.

Figure 4(b) depicts the energy band structure obtained by diagonalizing the Hamiltonian Eq. (2). The parameters are set to be $t_1 = 1.0$, $t_2 = 0.6$, $s = 0.6$, $\delta = 0.2$, and $\Delta = 1.5$. On the other hand, the broken lines show the energy band structure in the case that the dimers are equivalent, where the parameters are set to be $t_1 = t_2 = 1.0$, $s = 0.6$, $\delta = 0.0$, and $\Delta = 1.5$. The energy bands split to those with up and down spins as expected. Under the condition that the system is commensurately filled (i.e., three-quarter, half, and quarter filling), the system under DAF order can be an insulator, and the zero net magnetization is realized because the numbers of occupied electrons with up and down spins are same.

Because dimers I and II are inequivalent after the structural phase transition, (EDO-TTF-I)₂ClO₄ will exhibit compensated ferrimagnetism if appropriate antiferromagnetic order occurs. I note the related organic compound (EDO-TTF-I)₂PF₆ has similar crystal structures; however, all the dimers are equivalent.[89]

2.2 Low-energy effective model of (EDO-TTF-I)₂ClO₄

In order to analyze the electronic state of (EDO-TTF-I)₂ClO₄ in low temperature, I construct the low energy effective model based on density functional theory (DFT). I use the program “Quantum ESPRESSO [90]” to obtain the energy band structure based on the DFT. In this research, the optimized norm-conserving Vanderbilt pseudopotentials and plane-wave basis sets [91, 92] are employed. In this research, the generalized gradient approximation suggested by Perdew, Burke, and Ernzerhof [93] is used as the exchange-correlation functional. The cut-off energy of the wave functions and charge densities are set to be 80 Ry and 320 Ry, respectively. I use a $5 \times 5 \times 3$ uniform \mathbf{k} -point grid and Methfessel-Paxton smearing method in the self-consistent calculation. This first-principles calculation is performed based on the crystal structure data analyzed in 100 K [21], however internal coordinates of H atoms are optimized. The following calculations are based on the relaxed crystal structure. Figure 5 (b) shows the energy band structure of (EDO-TTF-I)₂ClO₄ obtained by DFT. The four bands around E_F are isolated from the other energy bands in Fig. 5 (b). Therefore, I select them as the low energy degrees of freedom and calculate the wave functions of the Wannier orbitals using RESPACK [94]. The Wannier orbitals are shown in Fig.5 (a). Colors of anions mean their orientations in Fig. 5 (a). Because of the different configurations of ClO₄, dimer I and II become inequivalent. The inversion centers are located at the centers of each dimer. The eigenvalues of the tight-binding Hamiltonian described

by the Wannier orbitals (A, A', B, B') reproduce the original DFT band structures (Fig.5 (b)).

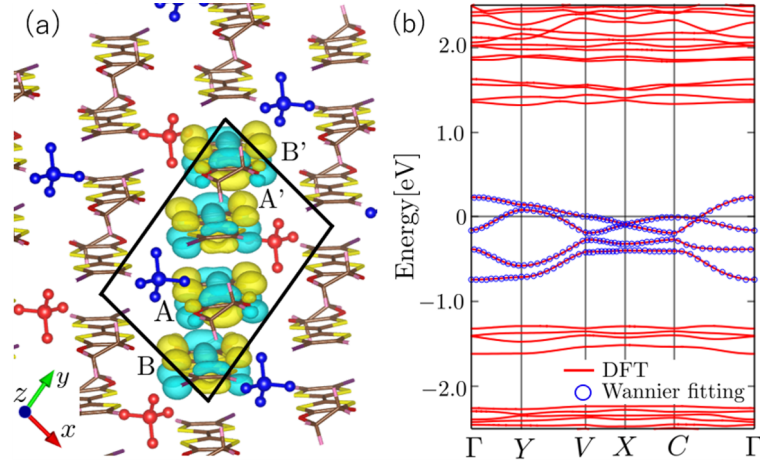


Figure 5: (a) Crystal structure of (EDO-TTF-I)₂ClO₄ at $T = 100$ K and the Wannier orbitals are drawn using VESTA [95]. The black frame shows an unit-cell containing four EDO-TTF-I molecules. Colors of anions ClO₄ illustrate their orientations, which make two dimers (A-A' and B-B') inequivalent. (b) Energy band structure obtained by first-principles calculation is shown by the red lines. The energy eigenvalues obtained by Wannier fitting are shown by the blue circles. E_F is set as the origin of energy.

Next, I introduce a low-energy effective model :

$$\begin{aligned}
 H &= H_0 + H_{\text{int}}, \\
 H_0 &= \sum_{i,j,\alpha,\beta,\sigma} t_{i\alpha j\beta} c_{i\alpha\sigma}^\dagger c_{j\beta\sigma}, \\
 H_{\text{int}} &= \sum_{i,\alpha} U_{i\alpha} n_{i\alpha\uparrow} n_{i\alpha\downarrow} + \frac{1}{2} \sum_{i,j,\alpha,\beta} V_{i\alpha j\beta} N_{i\alpha} N_{j\beta}. \quad (5)
 \end{aligned}$$

$c_{i\alpha\sigma}^\dagger$ and $c_{i\alpha\sigma}$ is creation and annihilation operators for an electron in the unit cell i with orbital α ($= A, A', B, B'$) and spin σ ($= \uparrow, \downarrow$). The charge density operator are given by $n_{i\alpha\sigma} = c_{i\alpha\sigma}^\dagger c_{i\alpha\sigma}$ and $N_{i\alpha} = n_{i\alpha\uparrow} + n_{i\alpha\downarrow}$. The transfer integrals $t_{i\alpha j\beta}$ are estimated by using the wave functions of Wannier orbitals. I also calculate the Coulomb interactions $U_{i\alpha}$ and $V_{i\alpha j\beta}$ incorporating screening effect by the constrained random phase approximation (cRPA) [96, 97] implemented in RESPACK [94]. The cutoff energy of the polarization functions is set to be 5.0 Ry. I summarize the transfer integrals whose absolute values are larger than 0.020 eV and the Coulomb interactions in Table 1. The cutoff energy of the Coulomb interaction is set to be 0.60 eV. They are schematically illustrated in Fig. 6.

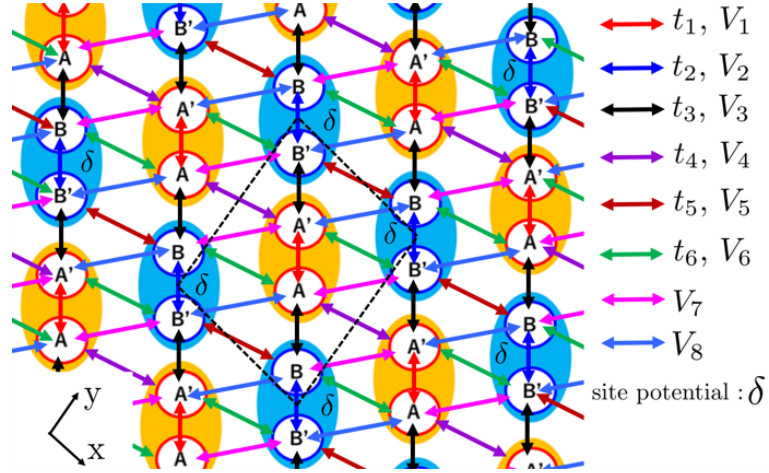


Figure 6: Transfer integrals and the neighbor Coulomb interactions are schematically illustrated.

Transfer integrals [eV]		Coulomb interactions [eV]	
δ	0.047	$U_A^{\text{res}}=U_{A'}^{\text{res}}$	2.094
		$U_B^{\text{res}}=U_{B'}^{\text{res}}$	2.076
t_1	0.252	V_1^{res}	0.903
t_2	0.179	V_2^{res}	0.884
t_3	0.128	V_3^{res}	0.880
t_4	0.112	V_4^{res}	0.700
t_5	0.084	V_5^{res}	0.681
t_6	0.058	V_6^{res}	0.614
t_7	-	V_7^{res}	0.659
t_8	-	V_8^{res}	0.628

Table 1: Numerical data of transfer integrals(> 0.020 eV) and screened Coulomb interactions.

Actually, I subtract the dimensional downfolding shift value Δ_{DDF} from the Coulomb repulsion parameters evaluated by RESPACK to incorporate the screening effect between the layers in the following calculations. [98, 99]. Following the previous researches [99, 100, 101, 102], I set $\Delta_{\text{DDF}} = 0.2$ eV. I confirm that the qualitative results are hardly influenced by Δ_{DDF} .

2.3 Hartree-Fock approximation (HFA)

To determine the candidate ground state for (EDO-TTF-I)₂ClO₄, I perform a real-space Hartree-Fock approximation (HFA) to the low-energy effective model. I use the unrestricted Hartree-Fock (UHF) program equipped in mVMC [88]. The initial variational parameters for the mVMC are generated from real-space HFA results. In this study, I consider the ordered states that do not change the periodicity of the crystal. I attempt five initial states as shown in Fig. 7 : (i) the paramagnetic (PM) state, (ii) the ferromagnetic (FM) state, (iii) the dimer antiferromagnetic (DAF) state, (iv) the AF state, (v) the AF state with charge order (AF+CO). To investigate the electron correlation effects in detail, I introduce the parameters λ and Δ_{DDF} . λ tunes the Coulomb interaction parameters. Δ_{DDF} is a dimension downfolding shift value which incorporates the screening effects via different layers [98, 99]. Using these parameters, I express $U_{i\alpha}$ and $V_{i\alpha j\beta}$ as $U_{i\alpha} \equiv \lambda(U_{i\alpha}^{\text{res}} - \Delta_{\text{DDF}})$ and $V_{i\alpha j\beta} \equiv \lambda(V_{i\alpha j\beta}^{\text{res}} - \Delta_{\text{DDF}})$. Figures 8 (a) and (b) show the behaviors of the charge density $\langle n_i^{\text{C}} \rangle = \langle n_{i\uparrow} \rangle + \langle n_{i\downarrow} \rangle$ and spin density $\langle n_i^{\text{S}} \rangle = \langle n_{i\uparrow} \rangle - \langle n_{i\downarrow} \rangle$ for the orbital i . The horizontal axis indicates λ . Δ_{DDF} is set to be 0.2 eV then. In $\lambda \lesssim 0.3$, PM state [$\langle n_{A(B)}^{\text{C}} \rangle = \langle n_{A'(B')}^{\text{C}} \rangle$ and $\langle n_i^{\text{S}} \rangle = 0$] is the ground state. In $0.3 \lesssim \lambda \lesssim 0.5$, DAF order [$\langle n_{A(B)}^{\text{C}} \rangle = \langle n_{A'(B')}^{\text{C}} \rangle$ and $\langle n_A^{\text{S}} \rangle = \langle n_{A'}^{\text{S}} \rangle = -\langle n_B^{\text{S}} \rangle = -\langle n_{B'}^{\text{S}} \rangle$] appears as the ground state. In $\lambda \gtrsim 0.5$, the AF+CO [$\langle n_{A(B')}^{\text{C}} \rangle > \langle n_{A'(B)}^{\text{C}} \rangle$ and $\langle n_{A'(B')}^{\text{S}} \rangle > \langle n_{A(B)}^{\text{S}} \rangle$] is obtained. The λ - Δ_{DDF} phase diagram is also shown in Fig. 8 (c). Because magnitudes of $U_{i\alpha}$ and $V_{i\alpha j\beta}$ decrease as Δ_{DDF} increases, the phase boundary between the DAF and AF+CO states slightly changes with Δ_{DDF} .

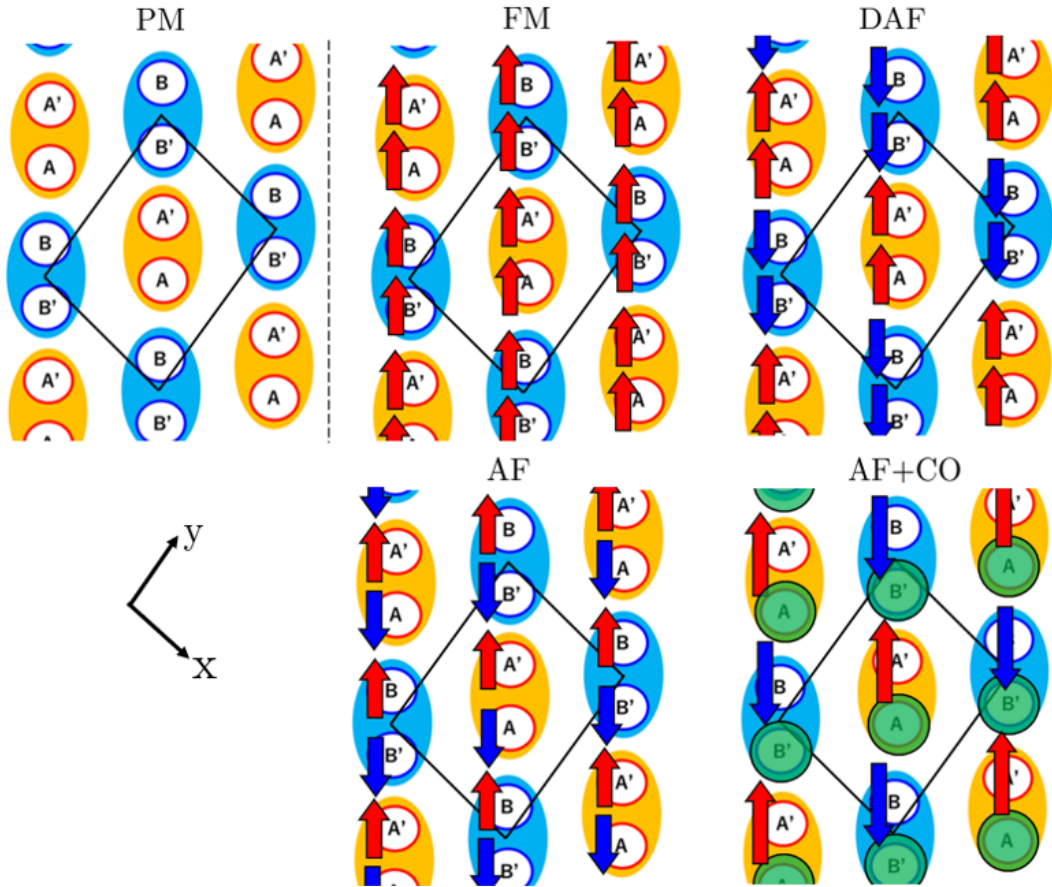


Figure 7: Initial states for in real-space HFA. The orange and blue ellipses represent the dimer I and II, respectively. The green circles show the charge-rich sites.

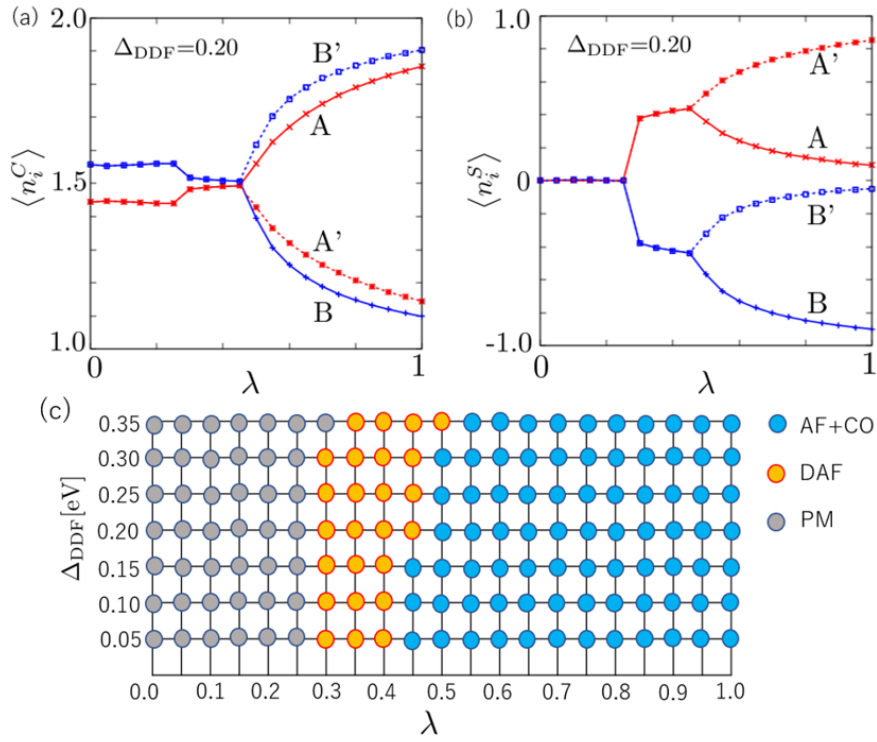


Figure 8: Behaviors of (a) $\langle n_i^C \rangle$ and (b) $\langle n_i^S \rangle$ to the parameter λ . (c) λ - Δ_{DDF} phase diagram obtained by real space HFA.

2.4 Many-variable variational Monte Carlo (mVMC) analysis

The variational method approximately determines the wave function of the ground state by optimizing variational parameters so that the energy expectation value is minimized. The variational method in condensed matter physics requires summation over real-space configurations $|x\rangle$ when calculating energy expectation values, which needs enormous numerical costs. Therefore, the variational Monte Carlo method evaluates the physical quantities, such as energy expectation value, using Markov chain Monte Carlo sampling in the summation over $|x\rangle$. The key to obtaining highly accurate wave functions at realistic computational cost in variational method and variational Monte Carlo methods is the setting of the trial wave function.

Gutzwiller employed the trial wave function that multiplies the Slater determinant of plane wave state by the Gutzwiller factor in order to investigate the ferromagnetism on transition metal[103]. Then, he used an approximation (Gutzwiller approximation, GA) in which up-spin and down-spin electrons are treated independently and energy expectation values are calculated probabilistically. Gutzwiller's theory attracted attention in terms of MI transition. Brinkman and Rice researched MI transition in the half-filled Hubbard model using Gutzwiller wave function (GWF)[104] and GA. Under the GA, it is shown that MI transition occurs. Later, however, Yokoyama and Shiba used a variational Monte Carlo method as a calculation beyond GA and showed that GWF describes only the metallic state in a finite-dimensional model and cannot explain MI transition[105]. Brinkman and Rice's theory is justified only for infinite-dimensional systems. Cappelo et al. calculated some physical quantities in the finite-dimensional Hubbard model, such as the energy expectation value, spin correlation function, and density correlation function, using the trial wave function that multiples GWF by Jastrow correlation factor[106] (GWF+J)[107]. In the result, they explained that MI transition in finite dimensional model. Jastrow correlation factor incorporate the effect of charge density fluctuations and greatly reduces the energy in the strongly correlated regime, and in $U \rightarrow \infty$, it reproduces the energy of the exact solution of the Heisenberg model with good accuracy, successfully describing the insulating state. Furthermore, the theory shows that by considering next-nearest neighbor transfer integrals, a metal-insulator transition from a spin-gapped metal to a dimerized insulator can occur.

Because of this history, not only the Gutzwiller factor but also the Jastrow factor is considered important in variational Monte Carlo methods for strongly correlated systems. Moreover, Jastrow is considered to be even more important because the model treated in this study also takes into account neighbor Coulomb interaction and far transfer.

I solve the low energy effective model using the mVMC method [87, 88],

which can consider quantum fluctuations and spatial correlations seriously. In this research, I use the following trial wave function :

$$|\psi\rangle = \mathcal{P}_G \mathcal{P}_J \mathcal{L}_S |\phi_{pair}\rangle, \quad (6)$$

$$\mathcal{P}_G = \exp \left[\sum_i g_i n_{i\uparrow} n_{i\downarrow} \right], \quad (7)$$

$$\mathcal{P}_J = \exp \left[\frac{1}{2} \sum_{i \neq j} v_{ij} N_i N_j \right], \quad (8)$$

$$|\phi_{pair}\rangle = \left[\sum_{i,j}^{N_{site}} f_{ij} c_{i\uparrow}^\dagger c_{j\downarrow}^\dagger \right]^{N_e/2} |0\rangle, \quad (9)$$

where \mathcal{P}_G , \mathcal{P}_J , and \mathcal{L}_S are the Gutzwiller factor [103], long-range Jastrow factor [106, 107], and total spin projector [108, 109], respectively [88, 110]. \mathcal{L}_S is important in the case of short-range correlations such as the one-dimensional antiferromagnetic Heisenberg spin model and spin singlet. Since theoretical predictions have shown that spin singlet is formed under CO order in organic conductors α -(BEDT-TTF)₂I₃ [101], this study takes such a possibility into account and performs spin projection. In conclusion, however, the ground state of this system is long-range magnetic order, and the effect of \mathcal{L}_S is not very important for the present study. N_e and N_{site} denote the numbers of electrons and sites, respectively. In the numerical calculation, 1×4 sublattice structure is imposed on variational parameters. In addition, I also perform an electron-hole transformation to save costs for the calculations. I employ the results obtained by the HFA as the initial f_{ij} value. I use the spin-singlet projection ($S = 0$) in the mVMC calculations for $L_x = L_y \leq 8$. Meanwhile, I don't use it for $L_x = L_y \geq 10$ to save the numerical costs. It is confirmed that the spin projection hardly influences physical quantities, such as the spin correlation functions. All variational parameters are simultaneously relaxed using the stochastic reconfiguration method [111].

According to the HFA, the DAF state (Fig.9 (a)) and AF+CO are obtained as the candidates of the ground state. Within the framework of the HFA, for $\lambda=1$, the AF+CO state is obtained as the ground state of the effective model. However, within the framework of the mVMC method, the DAF state is obtained as the ground state of the effective Hamiltonian. In addition, I confirm that the DAF state is obtained even if I use the variational parameters of AF+CO state as the initial state. These results mean that the electron correlation effect beyond the HFA makes the DAF state stable.

To show that the a long-range magnetic order exists, I calculate the spin-correlation functions, given by

$$S(\mathbf{q}) = \frac{1}{(N_{site})^2} \sum_{i,j} \langle \mathbf{S}_i \cdot \mathbf{S}_j \rangle e^{i\mathbf{q} \cdot (\mathbf{r}_i - \mathbf{r}_j)}. \quad (10)$$

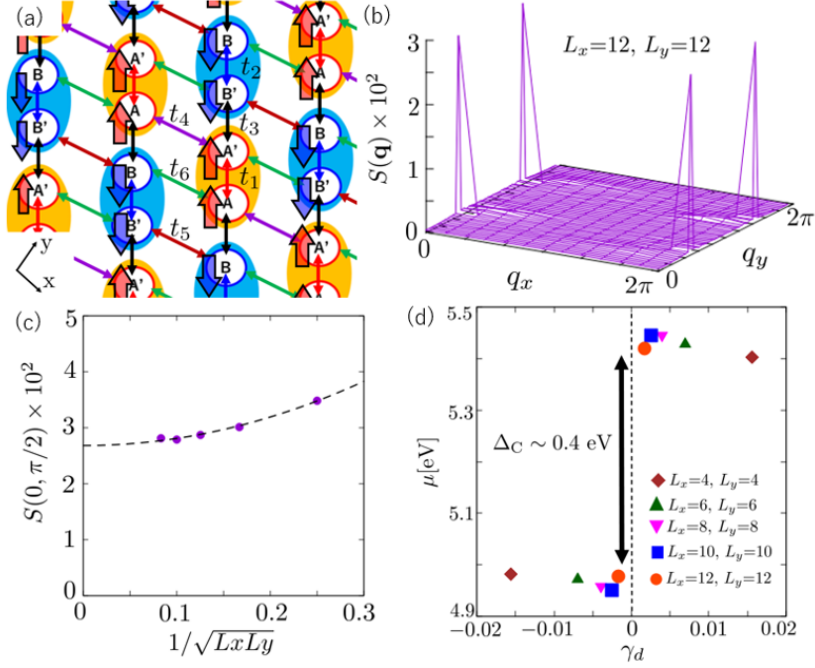


Figure 9: (a) DAF state and large transfer integrals t_1, t_2, \dots, t_6 are schematically illustrated in the two-dimensional conducting layer. (b) Spin correlation function obtained based on the mVMC method. It has the sharp peaks at $(q_x, q_y) = (0, \pi/2), (0, 3\pi/2)$. The system size is $L_x = 12$ and $L_y = 12$. (c) System size dependence of $S(0, \pi/2)$. (d) The chemical potential as a function of doping-rate γ_d .

For simplicity, $S(\mathbf{q})$ is mapped to the $L_x \times 4L_y$ square lattice. Figure 9 (b) depicts $S(\mathbf{q})$ in q_x - q_y plane. It has the sharp peaks at $(q_x, q_y) = (0, \pi/2)$ and $(q_x, q_y) = (0, 3\pi/2)$. In Fig. 9 (c), the peaks of $S(\mathbf{q})$ have finite values in the bulk limit. I also find that charge densities of all orbitals are almost 1.5 and a charge order does not appear. These results imply that the ground state of the effective model is the DAF state. Moreover, I calculate the charge gap Δ_c , defined as $\Delta_c = \mu(N_e + 1) - \mu(N_e - 1)$. The chemical potential is determined by $\mu(N_e + 1) = [E(N_e + 2) - E(N_e)]/2$. Figure 9 (d) displays the chemical potential as a function of doping rate γ_d ($=N_e/N_{\text{site}} - 1.5$). The charge gap is estimated as $\Delta_c \sim 0.4$ eV from Fig. 9. It shows that the DAF obtained as the ground state is an insulator.

Here, I show λ dependence of the ground state in Fig. 10 (a), where I set $\Delta_{DDF} = 0.2$ eV and $L_x = L_y = 6$. By increasing λ , the phase transition from PM state to DAF state occurs $\lambda \sim 0.5$. In $\lambda \sim 2.2$, the AF+CO state is stabilized because of neighbor Coulomb repulsion. Figure 10(b) shows difference of energies between the PM (AF+CO) and DAF states, i.e., λ dependence of $\Delta E_1 = E_{\text{PM}} - E_{\text{DAF}}$ ($\Delta E_2 = E_{\text{AF+CO}} - E_{\text{DAF}}$). Figure 11

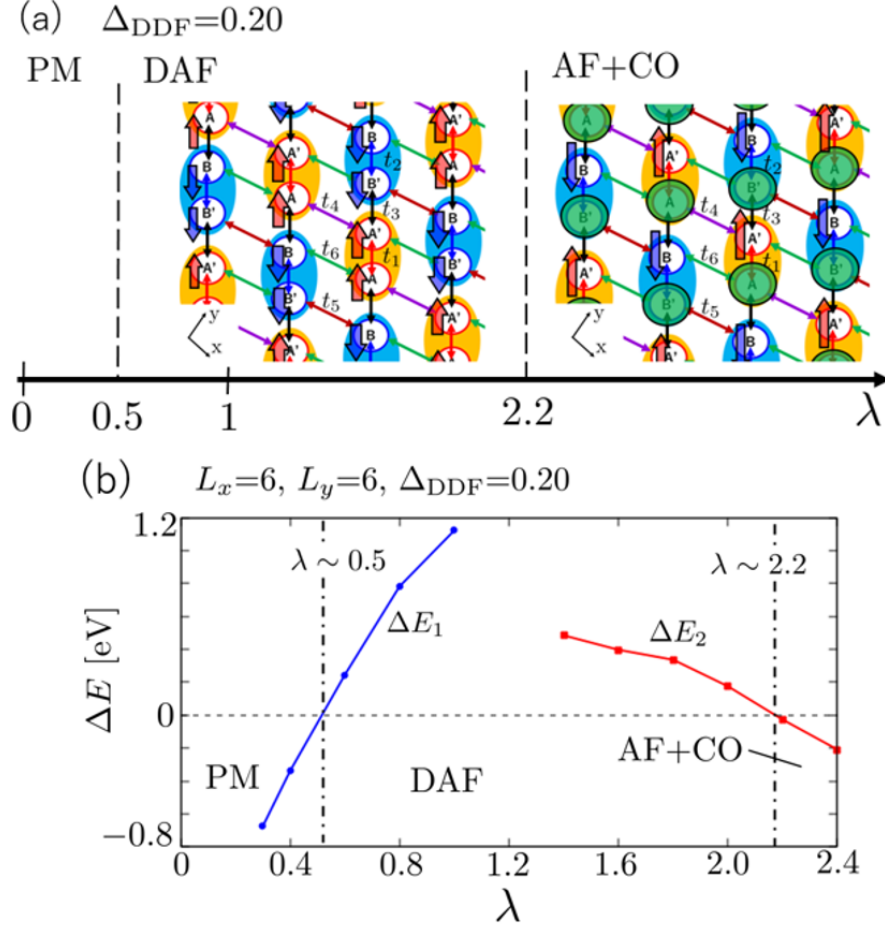


Figure 10: (a) λ phase diagram drawn based on the mVMC method. (b) ΔE_1 and ΔE_2 are shown as functions of λ .

depicts the spin and charge correlation functions of the PM, the DAF, and the AF+CO states. The charge correlation function is given by

$$N(\mathbf{q}) = \frac{1}{(N_{\text{site}})^2} \sum_{i,j} \langle (N_i - \bar{N}) \cdot (N_j - \bar{N}) \rangle e^{i\mathbf{q} \cdot (\mathbf{r}_i - \mathbf{r}_j)}, \quad (11)$$

$$\bar{N} = \frac{1}{N_{\text{site}}} \sum_i \langle N_i \rangle. \quad (12)$$

The peaks $S(0, \pi/2)$ and $S(0, 3\pi/2)$ in Fig. 11 (b) mean that the DAF state is stabilized. On the other hand, the peaks $S(0, \pi/2)$, $S(0, 3\pi/2)$ and $N(0, \pi)$ in Figs. 11(c) and (f) mean the AF+CO state is stabilized.

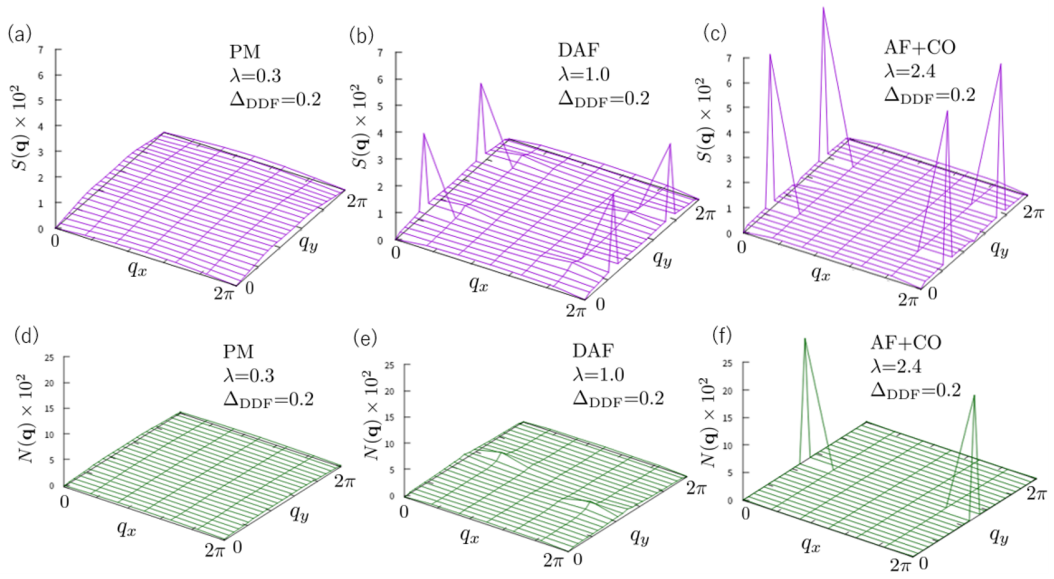


Figure 11: Spin correlation function $S(\mathbf{q})$ [density correlation function $N(\mathbf{q})$] of the PM state ($\lambda = 0.3$), the DAF state ($\lambda = 1$), and the AF+CO state ($\lambda = 2.4$) in (a), (b), and (c) [(d), (e), and (f)], respectively.

2.5 Analysis of the DAF state

Since the mVMC calculations yielded the DAF state as the ground state, I examine spin splitting phenomenon under the DAF order using the HFA. I impose the DAF order and tune λ , which controls U_i and $V_{i,j}$, to reproduce the charge gap $\Delta_c \sim 0.4$ eV estimated by the mVMC method. As a result, λ is estimated to be $\lambda = 0.7$. The mean-field Hamiltonian in the momentum picture is expressed by

$$\begin{aligned}
H^{\text{HFA}} = & \sum_{\mathbf{k}} \sum_{\delta, \alpha, \beta, \sigma} t_{\delta, \alpha \beta} e^{i\mathbf{k} \cdot \delta} c_{\mathbf{k}, \alpha, \sigma}^\dagger c_{\mathbf{k}, \beta, \sigma} \\
& + \sum_{\mathbf{k}} \sum_{\alpha, \sigma} U_\alpha \left\langle c_{\alpha, \bar{\sigma}}^\dagger c_{\alpha, \bar{\sigma}} \right\rangle c_{\mathbf{k}, \alpha, \sigma}^\dagger c_{\mathbf{k}, \alpha, \sigma} \\
& + \sum_{\mathbf{k}} \sum_{\delta, \alpha, \beta, \sigma} V_{\delta, \alpha \beta} \langle N_\beta \rangle c_{\mathbf{k}, \alpha, \sigma}^\dagger c_{\mathbf{k}, \alpha, \sigma} \\
& - \sum_{\mathbf{k}} \sum_{\delta, \alpha, \beta, \sigma} V_{\delta, \alpha \beta} \left\langle c_{\beta, \sigma}^\dagger c_{\alpha, \sigma} \right\rangle^{(\delta)} e^{i\mathbf{k} \cdot \delta} c_{\mathbf{k}, \alpha, \sigma}^\dagger c_{\mathbf{k}, \beta, \sigma}.
\end{aligned} \tag{13}$$

δ is the translational vector and $\bar{\sigma} = -\sigma$. I use the one-body Green's functions $\left\langle c_{\beta, \sigma}^\dagger c_{\alpha, \sigma} \right\rangle$ obtained by real-space HFA, which correspond to DAF state.

Using the Hamiltonian H^{HFA} , I calculate the density of state (DOS) and energy dispersion. DOS is given by $D_\sigma(\omega) = (\pi L_x L_y)^{-1} \sum_{\mathbf{k}, n} \text{Im}(\omega - i\eta - E_{\mathbf{k}, n, \sigma} + \mu)^{-1}$, where μ is the chemical potential and η takes an infinitesimal value. I set $\eta = 0.002$ eV in the numerical calculation. $E_{\mathbf{k}, n, \sigma}$ is the eigenvalue of H^{HFA} , where n is the band index. Fig. 12 (a) shows that DAF order causes spin splitting ($D_\uparrow(\omega) \neq D_\downarrow(\omega)$). Fig. 12(b) shows the energy dispersion under the DAF order. Spin splitting occurs on any momenta \mathbf{k} . These behaviors show that (EDO-TTF-I)₂ClO₄ can exhibit fully compensated ferrimagnetism under the DAF order.

Here, I examine the origin of spin splitting phenomenon in this material. As in the simple model, $t_- = (t_1 - t_2)/2$ and δ cause isotropic spin splitting. In this material, $t_- (= 0.036$ eV) and $\delta (= 0.047$ eV) are comparable, so both t_- and δ contribute to the spin splitting phenomenon. One might think that a finite δ would make the total magnetization finite, however, the charge gap ensures that the total magnetization is robust to perturbations. In this case, the total magnetization is zero at $\delta=0$ and remains zero even if δ is added, provided that δ is significantly smaller than the charge gap.

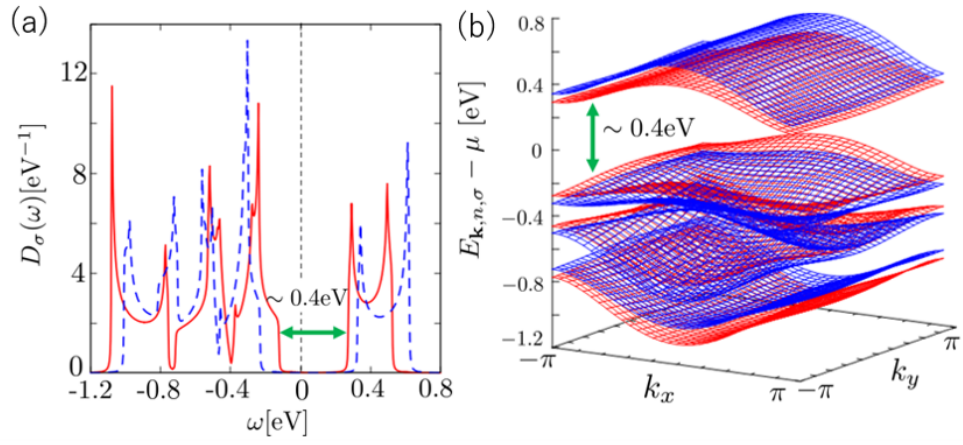


Figure 12: (a) DOS obtained by the mean-field Hamiltonian H^{HFA} . $D_{\uparrow}(\omega)$ and $D_{\downarrow}(\omega)$ are shown by red solid and blue broken lines. (b) Energy dispersion obtained by the mean-field Hamiltonian H^{HFA} . The red and blue bands display those with up and down spins, respectively.

2.6 Summary and discussion

In this study, I propose a simple method to realize fully compensated ferrimagnetism using molecular orbital degrees of freedom in organic materials. First, using a simple model, I show that two inequivalent dimers and DAF order induce fully compensated ferrimagnetism. I further propose that the ground state of $(\text{EDO-TTF-I})_2\text{ClO}_4$ is a DAF insulator where spins of the two inequivalent dimers are inversely correlated. As a result, the spin splitting phenomenon occurs under the DAF order. Incidentally, an organic material $(\text{EDO-TTF-I})_2\text{PF}_6$ with a crystal structure similar to $(\text{EDO-TTF-I})_2\text{ClO}_4$ has been found[89], however it does not become a compensated ferrimagnet since the all dimers in it are equivalent.

The key to fully compensated ferrimagnetism is that the anion ordering makes the two dimers inequivalent. The discovery of the compensated ferrimagnetism caused by inequivalent dimers as well as the potential for materials design using anion ordering, shows that organic compounds provide a various platform for investigating exotic magnetic properties. I expect that the doping effects will be examined in the DAF insulator in future work. It is predicted that the exotic physical phenomena, such as triplet superconductivity [112], are observed because of the polarized lowest unoccupied energy band and its large DOS as shown in Fig.12 (a). Further experimental and theoretical investigations in this direction are desirable.

3 Fragment-orbital-dependent spin fluctuations

Abstract

Motivated by ^{13}C nuclear magnetic resonance (NMR) experiments, I investigated the spin fluctuations enhanced in the single-component molecular conductor $[\text{Ni}(\text{dmdt})_2]$, which is the Dirac nodal line system. Especially, I calculated the spin susceptibility, Knight shift, and spin-lattice relaxation rate ($1/T_1T$) by applying the random phase approximation (RPA) to a Hubbard model which consists of three fragment orbitals and short-range Coulomb interaction evaluated by *ab initio* many-body perturbation theory calculations. I found that the commensurate ($\mathbf{q}=\mathbf{0}$) and incommensurate spin fluctuations are enhanced depending on the fragment orbitals. The commensurate and incommensurate responses contribute to $1/T_1T$ in low and high T in the presence of on-site Coulomb repulsion, respectively. I show that $1/T_1T$ decreases with cooling but turns to increase at low T due to the commensurate spin fluctuations. However, the Knight shift decreases with cooling. Such behaviors result from the characteristic wave functions of this Dirac nodal line system, which is expressed by an n -band ($n \geq 3$) model, causing intra-molecular antiferromagnetic fluctuations. I explain that the fragment orbitals substantially have a hand in the spin fluctuations and the physical quantities related to them in $[\text{Ni}(\text{dmdt})_2]$.

3.1 Low-energy effective model and formulation

I calculate the spin susceptibility to investigate the spin fluctuations in $[\text{Ni}(\text{dmdt})_2]$. I consider the electron correlation effect to the spin susceptibility in the framework of the perturbation theory. I also calculate the Knight shift and $1/T_1T$ for the respective fragment orbitals. They are the physical quantities measured by nuclear magnetic resonance (NMR). I use RPA to the multi-orbital Hubbard Hamiltonian to calculate the spin susceptibility in $[\text{Ni}(\text{dmdt})_2]$. Calculation methods considering the effect of self-energy, such as FLEX, have higher accuracy than RPA. However, I choose RPA as the method to treat the electron correlation because the quasi-particle peak spreading by self-energy tends to suppress spin fluctuations.

The Hubbard model is given by the following Hamiltonian :

$$H = \sum_{\langle i,\alpha;j,\beta \rangle,\sigma} t_{i,\alpha;j,\beta} c_{i,\alpha,\sigma}^\dagger c_{j,\beta,\sigma} + \sum_{i,\alpha} U_\alpha n_{i,\alpha,\uparrow} n_{i,\alpha,\downarrow}, \quad (14)$$

where i and j denote the unit-cell indices, and σ indicates the spin index (\uparrow or \downarrow). α and β stand for the fragment orbitals A, B, and C. $t_{i,\alpha;j,\beta}$ denotes a transfer integral between the orbitals α and β which belong to the unit-cells i and j . And, U_α is the on-site Coulomb interaction on the orbital α . $\sum_{\langle \dots \rangle}$ denotes a summation for the transfers which is larger than the cut-off energy E_{cut} ($=0.010$ eV).

I perform the first-principles calculations and Wannier fitting using the programs QUANTUM ESPRESSO[90] and RESPACK[94], respectively.[75] QUANTUM ESPRESSO is used for first-principles calculation based on the pseudopotential method in the previous study. RESPACK is employed for evaluating the transfer integrals and screened repulsive interaction. The effective model of $[\text{Ni}(\text{dmdt})_2]$ near E_F is described by three fragment Wannier orbitals as depicted in Fig. 14, which are calculated using Wannier fitting to three energy bands (DFT) near E_F [75]. Figure 13 (a) shows the energy band structure obtained by QUANTUM ESPRESSO. In Fig. 13 (b), Wannier fitting reproduces the original energy band structure of DFT.

Figure 14(a) and (b) display a $\text{Ni}(\text{dmdt})_2$ molecule and fragment orbitals. The orbital B in Fig. 14(a) may look like a d symmetric orbital, but it is an anti-bonding state of p orbitals of the S atoms, as is evident from Fig. 14 (b). The d orbital of Ni doesn't greatly contribute to the orbital B. Meanwhile, the orbitals A and C are p symmetric. They are equivalent because the system has space-inversion symmetry. The three fragment orbitals are localized on the same molecule and belong to the same unit cell.

The Hamiltonian (Eq. 14) in the real space picture is converted to that in the momentum space picture by the Fourier transform :

$$H = \sum_{\mathbf{k},\alpha,\beta,\sigma} H_{\alpha\beta,\sigma}^0(\mathbf{k}) c_{\mathbf{k},\alpha,\sigma}^\dagger c_{\mathbf{k},\beta,\sigma} + \frac{1}{N_L} \sum_{\mathbf{k},\mathbf{k}',\mathbf{q},\alpha} U_{\alpha\alpha} c_{\mathbf{k}+\mathbf{q},\alpha,\uparrow}^\dagger c_{\mathbf{k}'-\mathbf{q},\alpha,\downarrow}^\dagger c_{\mathbf{k}',\alpha,\downarrow} c_{\mathbf{k},\alpha,\uparrow}. \quad (15)$$

\mathbf{k} , \mathbf{k}' , and \mathbf{q} are the three-dimensional wavenumber vectors. N_L denotes the system size (the number of the unit cells). In this study, I treat the first and second terms as unperturbed and perturbed Hamiltonians. Here, $H_{\alpha\beta,\sigma}^0(\mathbf{k})$ is defined as

$$H_{\alpha\beta,\sigma}^0(\mathbf{k}) = \sum_{\langle \delta \rangle} t_{\alpha\beta,\delta} e^{i\mathbf{k}\cdot\delta}. \quad (16)$$

δ is a translational vector. Further, $t_{\alpha\beta,\delta}$ indicates the transfer integrals, which are assigned to t_1, t_2, \dots, t_{12} and the site potential Δ , which is defined

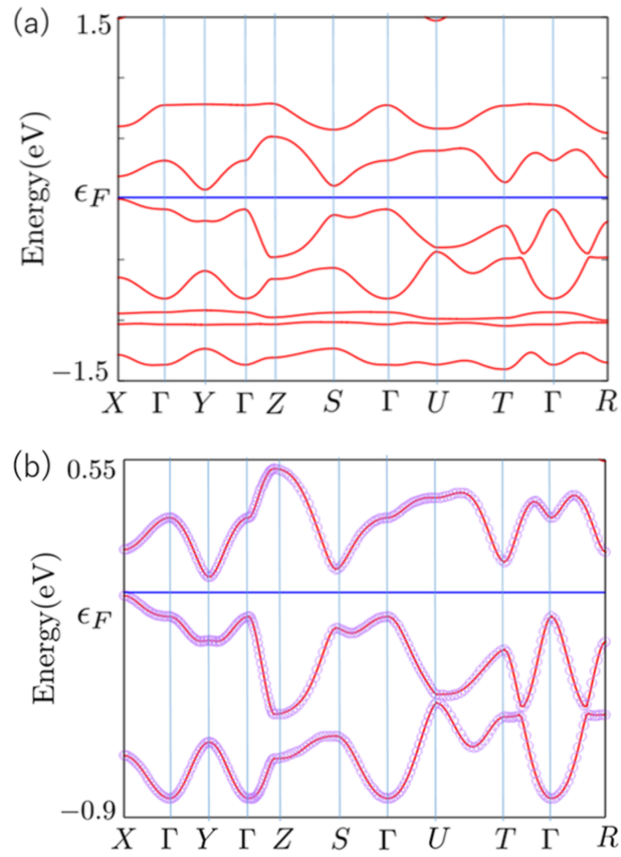


Figure 13: (a) Energy band structure of $[\text{Ni}(\text{dmdt})_2]$ obtained by DFT. (b) The energy eigenvalues calculated by Wannier fitting (purple circles) reproduce the original band structure of DFT (red lines).

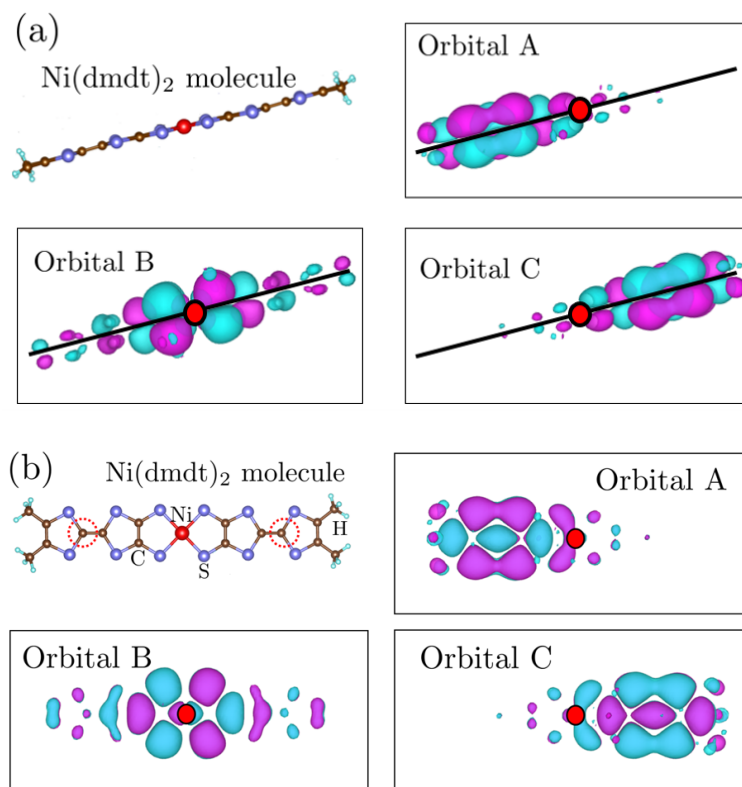


Figure 14: $\text{Ni}(\text{dmdt})_2$ molecule and the fragment orbitals A, B, and C are schematically shown. Ni, S, C, and H atoms are illustrated by red, blue, brown, and cyan balls, respectively. The red dots in respective fragment orbitals depict the position of the Ni atom for guiding eyes. (a) The view seen from the side of the molecule. The black solid lines illustrate the $\text{Ni}(\text{dmdt})_2$ molecule. (b) View of the molecule seen vertically. The red dotted circles enclose C atoms, which are substituted with ^{13}C in the ^{13}C -NMR experiment.[81, 82]

as the difference between the chemical potentials of the orbitals A and B $\Delta \equiv t_{BB,0} - t_{AA,0}$, in Table 2. Note that the small transfer integrals whose absolute values are less than a cutoff (0.010 eV) are omitted for simplicity (Fig. 15). t_1 links the nearest neighbor fragment orbitals within a molecule. t_2, t_3, \dots, t_8 connect those between molecules in the b - c plane which is the main conduction plane. The transfer integrals t_1, t_2 , and t_3 are essential to generate the linear dispersions (Dirac cones). Meanwhile, t_9 creates Fermi surfaces along the nodal line. In addition, t_{10}, t_{11} , and t_{12} wind the nodal lines.

transfer integrals (eV)	
t_1	-0.2372
t_2	-0.1840
t_3	-0.2080
t_4	0.0302
t_5	0.0326
t_6	-0.0389
t_7	0.0103
t_8	-0.0144
t_9	-0.0140
t_{10}	-0.0541
t_{11}	-0.0534
t_{12}	0.0116
site potential (eV)	
Δ	0.0429

Table 2: Numerical data of transfer integrals and site potential are shown.

In the previous study, I calculated some physical quantities of $[M(\text{dmdt})_2]$ ($M = \text{Pt}, \text{Ni}$) incorporating the spin-orbit coupling (SOC) as a parameter modulating the imaginary parts of the transfer integrals. I found that the SOC can shrink the size of the Fermi surface.[74, 75] The energy scale of SOC in $[\text{Ni}(\text{dmdt})_2]$ (~ 0.0016 eV) was estimated to be substantially smaller than that of the Fermi surface (~ 0.01 eV)[75]. Thus, it is considered that SOC in reality should not be large enough to greatly contribute to the Knight shift and $1/T_1T$. In this research, I disregard the effect of SOC.

From the definition in Eq. 16, the matrix elements of the unperturbed

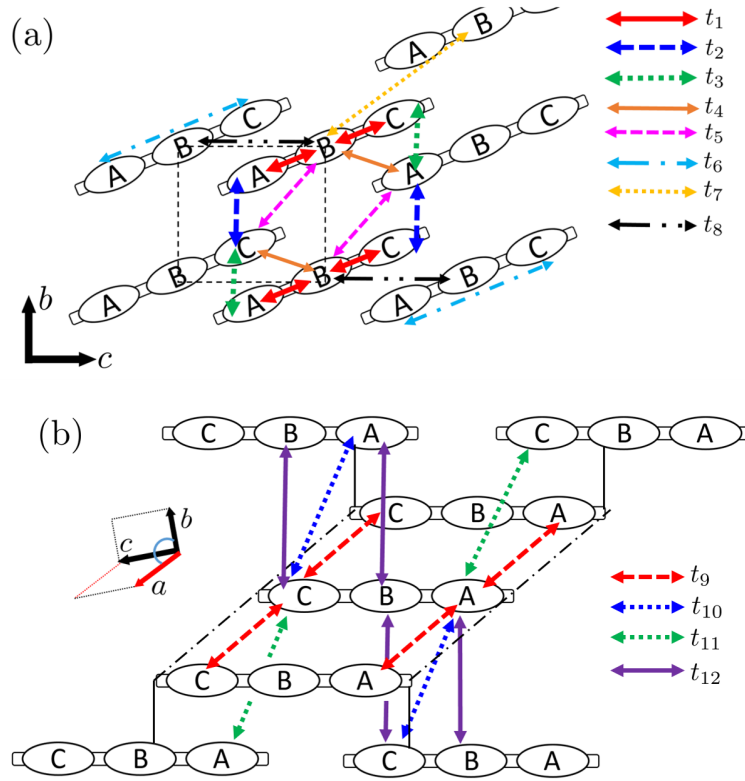


Figure 15: The relationship between transfer integrals and the fragment orbitals is schematically shown. (a) Two-dimensional network the hopping (shown by double-headed arrows) in b - c plane is schematically illustrated. The unit cell is represented by the dashed square. (b) The three-dimensional network containing the hopping in the a -direction is schematically illustrated. The black chain and vertical bold lines in (b) are for guiding eyes. The former lines are parallel to the a -direction. The latter lines connect the molecules in the identical b - c plane.

Hamiltonian $H_{\alpha\beta,\sigma}^0(\mathbf{k})$ are described by the following equations.

$$\begin{aligned}
H_{AA,\sigma}^0(\mathbf{k}) &= 2t_9 \cos k_a, \\
H_{AB,\sigma}^0(\mathbf{k}) &= t_{12}e^{i(-k_a+k_b+k_c)} + t_1 \\
&\quad + t_5e^{i(k_b+k_c)} + t_4e^{ik_c}, \\
H_{AC,\sigma}^0(\mathbf{k}) &= t_{10}e^{i(-k_a+k_b+k_c)} + t_{11}e^{i(k_a+k_c)} + t_6 \\
&\quad + t_3e^{ik_c} + t_2e^{i(k_b+k_c)}, \\
H_{BB,\sigma}^0(\mathbf{k}) &= \Delta + 2t_7 \cos(k_b + k_c) + 2t_8 \cos k_c, \\
H_{BC,\sigma}^0(\mathbf{k}) &= t_{12}e^{i(-k_a+k_b+k_c)} + t_1 \\
&\quad + t_5e^{i(k_b+k_c)} + t_4e^{ik_c}, \\
H_{CC,\sigma}^0(\mathbf{k}) &= 2t_9 \cos k_a.
\end{aligned} \tag{17}$$

In the following calculations, the system is treated as the cubic lattice where the lattice constant is 1. And, the system is also 2/3 filling because two of the three bands treated in the effective model are occupied.[74] The unperturbed Hamiltonian $\hat{H}_\sigma^0(\mathbf{k})$ satisfies the eigenvalue equation

$$\hat{H}_\sigma^0(\mathbf{k}) |\mathbf{k}, n, \sigma\rangle = E_{n,\sigma}(\mathbf{k}) |\mathbf{k}, n, \sigma\rangle, \tag{18}$$

$$|\mathbf{k}, n, \sigma\rangle = \begin{pmatrix} d_{A,n,\sigma}(\mathbf{k}) \\ d_{B,n,\sigma}(\mathbf{k}) \\ d_{C,n,\sigma}(\mathbf{k}) \end{pmatrix}. \tag{19}$$

$\hat{H}_\sigma^0(\mathbf{k})$ in Eq. 18 is comprised of $H_{\alpha\beta,\sigma}^0(\mathbf{k})$ in Eqs. 15 and 17. $E_{n,\sigma}(\mathbf{k})$ is the eigenvalue and $|\mathbf{k}, n, \sigma\rangle$ is the eigenvector where n indicates the band index. $d_{\alpha,n,\sigma}(\mathbf{k})$ is the matrix element of the unitary matrix, which corresponds to the wave functions. Because the effective model is 2/3 filling, the chemical potential μ is obtained by

$$\frac{1}{N_L} \sum_{\mathbf{k},n,\sigma} f_{\mathbf{k},n,\sigma} = 4, \tag{20}$$

$$\epsilon_{\mathbf{k},n,\sigma} \equiv E_{n,\sigma}(\mathbf{k}) - \mu, \tag{21}$$

$f_{\mathbf{k},n,\sigma} = 1/[1 + \exp(\epsilon_{\mathbf{k},n,\sigma}/T)]$ is the Fermi distribution function. At $T=0$, μ is equal to the Fermi energy E_F .

As the perturbed Hamiltonian in Eq. 15, I introduce the onsite Coulomb interaction $U_{\alpha\alpha}$ described by the fragment orbitals as a basis. The matrix expressing the onsite Coulomb interaction is given by

$$\begin{aligned}
\hat{U} &= \begin{pmatrix} U_{AA} & 0 & 0 \\ 0 & U_{BB} & 0 \\ 0 & 0 & U_{CC} \end{pmatrix} \\
&= \begin{pmatrix} \lambda U & 0 & 0 \\ 0 & U & 0 \\ 0 & 0 & \lambda U \end{pmatrix}.
\end{aligned} \tag{22}$$

The identity relation $U_{AA}=U_{CC}$ is satisfied due to the space-inversion symmetry. And, I introduce the controllable parameter $\lambda=U_{AA}/U_{BB}$. Using RESPACK, It is estimate that $U=6.72$ eV and $\lambda=0.79$ when the screening effect is not considered, and $U=2.68$ eV and $\lambda=0.95$ when it is considered. I employ $\lambda=0.95$ and U value less than 2.68 eV because RPA is apt to overestimate the effect of onsite Coulomb interaction.

In the framework of the linear response theory, the longitudinal and transverse spin susceptibilities are expressed by the equations :

$$\hat{\chi}^{zz}(\mathbf{q}, i\omega_l) \equiv \frac{1}{2} \int_0^{1/T} d\tau e^{i\omega_l \tau} \left\langle T_\tau \hat{S}_\mathbf{q}^z(\tau) \hat{S}_{-\mathbf{q}}^z(0) \right\rangle, \quad (23)$$

$$\hat{S}_\mathbf{q}^z = \frac{1}{N_L} \sum_{\mathbf{k}} \left(\hat{c}_{\mathbf{k}+\mathbf{q},\uparrow}^\dagger \hat{c}_{\mathbf{k},\uparrow} - \hat{c}_{\mathbf{k}+\mathbf{q},\downarrow}^\dagger \hat{c}_{\mathbf{k},\downarrow} \right), \quad (24)$$

$$\hat{\chi}^\pm(\mathbf{q}, i\omega_l) \equiv \int_0^{1/T} d\tau e^{i\omega_l \tau} \left\langle T_\tau \hat{S}_\mathbf{q}^+(\tau) \hat{S}_{-\mathbf{q}}^-(0) \right\rangle, \quad (25)$$

$$\hat{S}_\mathbf{q}^+ = \frac{1}{N_L} \sum_{\mathbf{k}} \hat{c}_{\mathbf{k}+\mathbf{q},\uparrow}^\dagger \hat{c}_{\mathbf{k},\downarrow}, \quad (26)$$

$$\hat{S}_{-\mathbf{q}}^- = \frac{1}{N_L} \sum_{\mathbf{k}} \hat{c}_{\mathbf{k},\downarrow}^\dagger \hat{c}_{\mathbf{k}+\mathbf{q},\uparrow}. \quad (27)$$

$i\omega_l=2li\pi T$ ($l \in \mathbf{Z}$) indicates the Matsubara frequency for boson and τ indicates the imaginary time. $\hat{S}_\mathbf{q}^z(\tau)$, $\hat{S}_\mathbf{q}^+(\tau)$, and $\hat{S}_{-\mathbf{q}}^-(\tau)$ are the spin operators expressed in the Heisenberg picture. The spin susceptibility is the proportionality coefficient of the magnetization to the infinitesimal magnetic field. It implies the degree of spin fluctuations because the response of spins to the infinitesimal magnetic field becomes sensitive under the circumstances that spin susceptibility has a large value.

By performing a perturbation expansion of Eqs. 23 and 25, the non-interacting longitudinal and transverse spin susceptibilities $\hat{\chi}^{zz,0}(\mathbf{q}, i\omega_l)$ and $\hat{\chi}^{\pm,0}(\mathbf{q}, i\omega_l)$ are obtained as the zeroth-order perturbation terms. In this study, SU(2) symmetry is protected in the paramagnetic state because the SOC and finite magnetic field are not imposed. Therefore, I define $\hat{\chi}^{zz,0}(\mathbf{q}, i\omega_l)=\hat{\chi}^{\pm,0}(\mathbf{q}, i\omega_l)\equiv\hat{\chi}^0(\mathbf{q}, i\omega_l)$. Its matrix elements are written as

$$\begin{aligned} \chi_{\alpha\beta}^0(\mathbf{q}, i\omega_l) \\ = -\frac{T}{N_L} \sum_{\mathbf{k}, m} G_{\alpha\beta}^0(\mathbf{k} + \mathbf{q}, i\tilde{\omega}_m + i\omega_l) G_{\beta\alpha}^0(\mathbf{k}, i\tilde{\omega}_m), \end{aligned} \quad (28)$$

$$G_{\alpha\beta,\sigma}^0(\mathbf{k}, i\tilde{\omega}_l) = \sum_n d_{\alpha,n,\sigma}(\mathbf{k}) d_{\beta,n,\sigma}^*(\mathbf{k}) \frac{1}{i\tilde{\omega}_l - \epsilon_{\mathbf{k},n,\sigma}}. \quad (29)$$

Eq. 29 denotes the matrix elements of the non-interacting Matsubara Green's function. $i\tilde{\omega}_l=(2l+1)\pi T$ is the Matsubara frequency for fermions. I omit σ in Eq. 28 because $\epsilon_{\mathbf{k},n,\uparrow}=\epsilon_{\mathbf{k},n,\downarrow}$ is satisfied in Eq. 29. The longitudinal and transverse spin susceptibilities in RPA are expressed by the Feynman diagrams depicted in Fig. 16 (A) and (B), respectively. The

$$\begin{aligned}
\hat{\chi}^{zz,s}(\mathbf{q}, i\omega_l) = & \text{Diagram 1} - \text{Diagram 2} - \text{Diagram 3} \\
& + \text{Diagram 4} - \text{Diagram 5} - \text{Diagram 6} \dots \text{(a)} \\
\hat{\chi}^{\pm,s}(\mathbf{q}, i\omega_l) = & \text{Diagram 7} + \text{Diagram 8} \\
& + \text{Diagram 9} + \dots \text{(b)}
\end{aligned}$$

Figure 16: (A) Feynman diagram describing $\hat{\chi}^{zz,s}(\mathbf{q}, i\omega_l)$. (B) Feynman diagram describing $\hat{\chi}^{\pm,s}(\mathbf{q}, i\omega_l)$. The non-interacting Matsubara Green's functions, which denote the quasi-particles, are represented by the solid lines, while the interaction is shown by the dashed lines. The open circles connect the non-interacting Matsubara Green's functions and the interaction. The black dots indicate the spin operators.

first terms in the right-hand sides of diagrams (A) and (B) correspond to the terms $\hat{\chi}^{zz,0}(\mathbf{q}, i\omega_l) = \hat{\chi}^{\pm,0}(\mathbf{q}, i\omega_l) = \hat{\chi}^0(\mathbf{q}, i\omega_l)$ (Eq. 28). Because the longitudinal and transverse spin susceptibilities are calculated by running summations of the series of $\hat{U}\hat{\chi}^0(\mathbf{q}, i\omega_l)$ in RPA, they are written as

$$\begin{aligned}\hat{\chi}^{zz,s}(\mathbf{q}, i\omega_l) &= \hat{\chi}^{\pm,s}(\mathbf{q}, i\omega_l) \equiv \hat{\chi}^s(\mathbf{q}, i\omega_l) \\ &= \hat{\chi}^0(\mathbf{q}, i\omega_l)[\hat{I} - \hat{U}\hat{\chi}^0(\mathbf{q}, i\omega_l)]^{-1}\end{aligned}\quad (30)$$

where \hat{I} is the unit matrix.

I introduce the Stoner factor $\xi_s(\mathbf{q})$ evaluating the degree of spin fluctuations. $\xi_s(\mathbf{q})$ is given by the largest eigenvalue of the matrix $\hat{U}\hat{\chi}^0(\mathbf{q}, 0)$. In the three-band model, $\xi_s(\mathbf{q})$ and $\hat{\chi}^s(\mathbf{q}, 0)$ are connected by the relational expression

$$\hat{\chi}^s(\mathbf{q}, 0) = \frac{1}{(1 - \xi_s(\mathbf{q}))} \frac{\hat{\chi}^0(\mathbf{q}, 0)\hat{P}(\mathbf{q})}{(1 - \phi_1(\mathbf{q}))(1 - \phi_2(\mathbf{q}))}, \quad (31)$$

where $\xi_s(\mathbf{q})$, $\phi_1(\mathbf{q})$, and $\phi_2(\mathbf{q})$ are the maximum and other eigenvalues of $\hat{U}\hat{\chi}^0(\mathbf{q}, 0)$. $\hat{P}(\mathbf{q})$ is the adjugate matrix of $\hat{I} - \hat{U}\hat{\chi}^0(\mathbf{q}, 0)$. The eigenvalues of $\hat{U}\hat{\chi}^0(\mathbf{q}, 0)$ are smaller than 1 in the paramagnetic regime. In the case of $\xi_s(\mathbf{q}) \rightarrow 1$, the spin susceptibility $\hat{\chi}^s(\mathbf{q}, 0)$ diverges and a magnetic order whose the period corresponding to the wavenumber \mathbf{q} is induced.

The Knight shift, K , and the spin-lattice relaxation rate, $(1/T_1T)$, for the orbital α are expressed by[113]

$$K_\alpha \propto \sum_{\beta} \text{Re} [\chi_{\alpha\beta}^{zz}(\mathbf{0}, 0)], \quad (32)$$

$$(1/T_1T)_\alpha \propto \lim_{\omega \rightarrow +0} \left[\frac{1}{N_L} \sum_{\mathbf{q}} \frac{\text{Im}\chi_{\alpha\alpha}^{\pm}(\mathbf{q}, \omega)}{\omega} \right] \quad (33)$$

According to Eqs. 31 and 33, all the \mathbf{q} components for which $\xi_s(\mathbf{q})$ becomes close to 1 dominantly contribute to $1/T_1T$ because they provide large value with the spin susceptibility. In contrast to $1/T_1T$, the Knight shift is influenced by only $\mathbf{q}=\mathbf{0}$ that gives $\xi_s(\mathbf{q}) \sim 1$ (see Eq. 32).

Because the spin susceptibility in the real-frequency representation $\hat{\chi}^s(\mathbf{q}, \omega)$ is necessary to calculate $1/T_1T$, I calculate $\hat{\chi}^s(\mathbf{q}, \omega)$ by applying an analytic continuation to Eq. 30. Therefore, not only the Matsubara frequency representation but also the real-frequency representation is used in this research.

3.2 Numerical result in the case of $U = 0$

I calculate several physical quantities, such as energy dispersion, density of state, spin susceptibility, Knight shift, and $1/T_1T$, in the case of $U=0$. I

explain that the spin susceptibility in $[\text{Ni}(\text{dmdt})_2]$ greatly depends on the fragment orbitals.

I obtain the energy eigenvalues in the momentum space by diagonalizing $\hat{H}_\sigma^0(\mathbf{k})$ in Eq. 18. The energy dispersion in the k_b-k_c plane is shown in Fig. 17 (a), where k_a is set to be $-\pi/2$. In the two-dimensional momentum space (k_b-k_c), the Dirac cones appear between bands 1 and 2 near E_F , and between bands 2 and 3 beneath E_F . The Dirac points are gapless because of space-inversion symmetry.

Dirac nodal lines are drawn by the Dirac points between bands 1 and 2 connecting in the k_a direction. The Dirac nodal line in the first Brillouin zone is shown in the inset of Fig. 17 (b). As the component of wavenumber k_a varies, the positions of the Dirac points created by bands 1 and 2 vary in the k_b-k_c plane and draw Dirac nodal lines in the momentum space [Fig. 17 (b)]. The Dirac points shift up and down across E_F as k_a varies, which creates electron and hole surfaces around the nodal lines. This behavior is schematically illustrated in Fig. 17 (c). The Fermi surface is depicted in Fig. 17(b). The energy scale of the Fermi surface is approximately 0.010 eV.

I also calculate the density of states (DOS), $D_{\text{tot}}(\omega)$ which is given by a summation of a fragment-orbital dependent DOS, $D_\alpha(\omega)$, which is defined as

$$D_\alpha(\omega) = -\frac{1}{\pi N_L} \sum_{\mathbf{k}, \sigma} \text{Im} G_{\alpha\alpha, \sigma}^{R,0}(\mathbf{k}, \omega), \quad (34)$$

$$G_{\alpha\beta, \sigma}^{R,0}(\mathbf{k}, \omega) = \sum_n d_{\alpha, n, \sigma}(\mathbf{k}) d_{\beta, n, \sigma}^*(\mathbf{k}) \frac{1}{\omega - \epsilon_{\mathbf{k}, n, \sigma} + i\eta}. \quad (35)$$

$\hat{G}^{R,0}(\mathbf{k}, \omega)$ is the non-interacting retarded Green's function, where $\eta > 0$ takes the infinitesimal value. $D_{\text{tot}}(\omega)$ and $D_\alpha(\omega)$ are shown in Fig. 18. The DOS is linear to ω near E_F because this material has the linear energy dispersion in low energy region and the effect of transfer integrals along the nodal line direction is small. The finite DOS at E_F results from the Fermi surface created by the transfer in the nodal line direction.

In order to explain the fragment orbital-dependent spin fluctuations in this material, it is necessary to introduce the wave function of the Dirac nodal system. Figure 19 shows k_b-k_c dependence of the squared absolute value of the wave function for the orbital B and band 2, $|d_{B,2,\sigma}(\mathbf{k})|^2$. k_a is set to be $-\pi/2$. Note that the line segments connecting the positions of the Dirac points (illustrated with black lines in Fig. 19) have $|d_{B,2,\sigma}(\mathbf{k})|^2=0$, which I call the “zero region (ZR)” in this study. In contrast to orbital B, orbitals A and C have no ZR in their wavefunctions. A similar ZR was previously found in n -band ($n \geq 3$) organic Dirac electron system α -(BEDT-TTF) $_2$ I $_3$ ($n=4$)[51].

I calculate the non-interacting spin susceptibility $\hat{\chi}^0(\mathbf{q}, \omega)$ in order to determine the spin fluctuations enhanced in $[\text{Ni}(\text{dmdt})_2]$. The diagonal elements of the non-interacting spin susceptibility $\chi_{AA}^0(\mathbf{q}, 0)$, $\chi_{BB}^0(\mathbf{q}, 0)$,

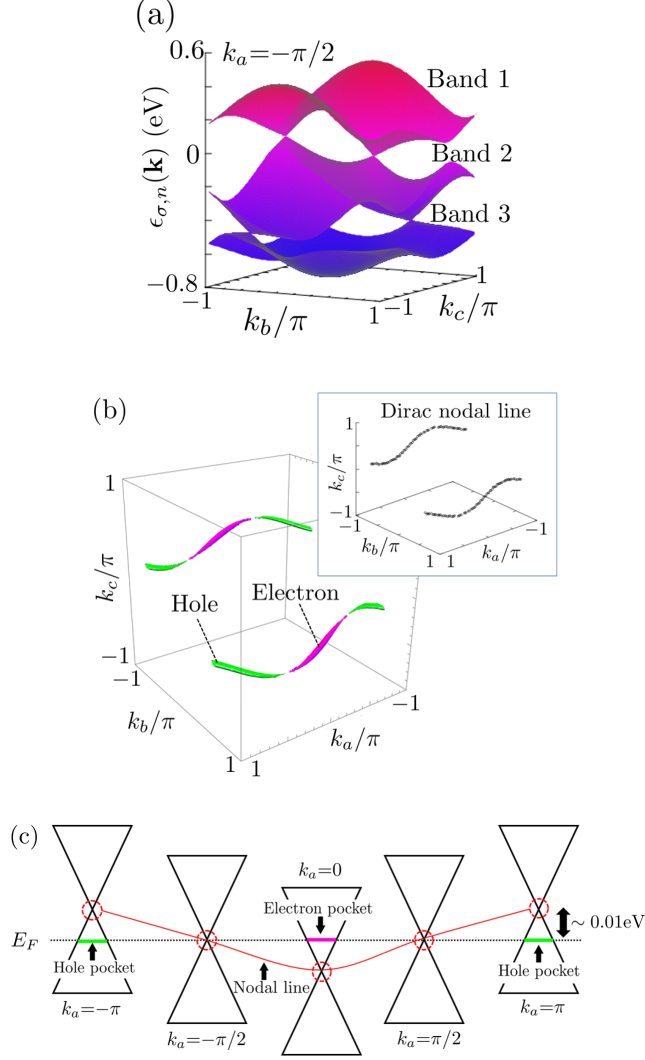


Figure 17: (a) Energy dispersion near E_F in the k_b - k_c plane. k_a is set to be $-\pi/2$. There are Dirac cones between each pair of bands. Dirac points between bands 1 and 2 depict the Dirac nodal lines in the momentum space. (b) Fermi surface in the first Brillouin zone. The electron and hole pockets are illustrated in magenta and green, respectively. The Dirac nodal lines in the first Brillouin zone are shown in the inset. (c) The relationship among the Dirac nodal line, Fermi surface, and wavenumber k_a is schematically shown. The red curved and dotted transverse lines indicate the Dirac nodal line and E_F , respectively.

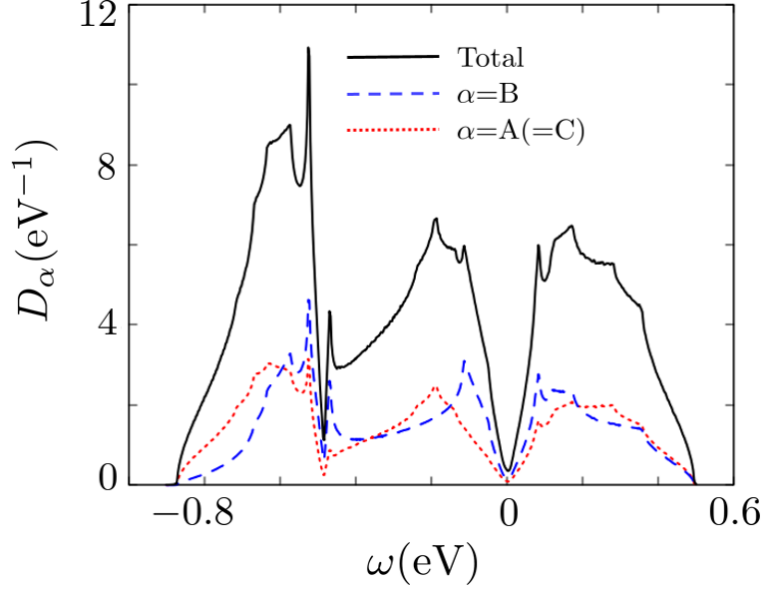


Figure 18: Total DOS and local DOS for the fragment orbital $\alpha=A(=C)$ and B are shown. $D_A(\omega)(=D_C(\omega))$, $D_B(\omega)$, and $D_{\text{tot}}(\omega)=\sum_{\alpha} D_{\alpha}(\omega)$ are shown by the red dotted and blue dashed, black solid lines, respectively.

$\text{Im}[\chi_{AA}^0(\mathbf{q}, \omega_0)]$, and $\text{Im}[\chi_{BB}^0(\mathbf{q}, \omega_0)]$ are in Fig. 20 (a), (b), (c), and (d), respectively. Temperature is set to be $T=0.003$ eV. These quantities increase with rising temperature at $\mathbf{q}=\mathbf{0}$. $\chi_{\alpha\alpha}^0(\mathbf{q}, 0)$ is a real number. I set $\omega_0=0.001$ eV because the imaginary part of the spin susceptibility at the infinitesimal frequency is needed to calculate Eq. 33. One of q_a , q_b , and q_c have to be fixed to illustrate the spin susceptibilities in the three-dimensional figures. I confirm that $\chi_{AA}^0(\mathbf{q}, 0)$ and $\chi_{BB}^0(\mathbf{q}, 0)$ have the maximum values at the commensurate wavenumber $\mathbf{q}=\mathbf{0}$ and the incommensurate wavenumber $\mathbf{q}=\mathbf{Q}=(0.20\pi, 0.73\pi, 0.58\pi)$ at $T=0.003$ eV. Therefore, I fix $q_a=0$ in Fig. 20 (a) and (c) and $q_a=0.2\pi$ in Fig. 20 (b) and (d). \mathbf{Q} is the wavenumber where $\chi_{BB}^0(\mathbf{q}, 0)$ has the maximum values and varies slightly with temperature. Although $\text{Im}[\chi_{BB}^0(\mathbf{q}, \omega_0)]$ has the maximum value $\mathbf{q}=\mathbf{Q}$ in Fig. 20 (d), $\text{Im}[\chi_{BB}^0(\mathbf{0}, \omega_0)]$ is largest in the entire Bz. It contributes to $(1/T_1T)_B$ in the case of $U=0$. $\chi_{CC}^0(\mathbf{q}, 0)$ is equal to $\chi_{AA}^0(\mathbf{q}, 0)$ due to space-inversion symmetry.

Such fragment-orbital dependencies of the spin susceptibilities imply that this material has two candidates for spin fluctuations which can be enhanced in the bulk. They are the spin fluctuations related to $\mathbf{q}=\mathbf{0}$ magnetic order and SDW. To investigate the reason why the spin susceptibilities in the momentum space depend on the fragment orbitals, the information about the spectral weights at E_F is essential. The spectral weight in the

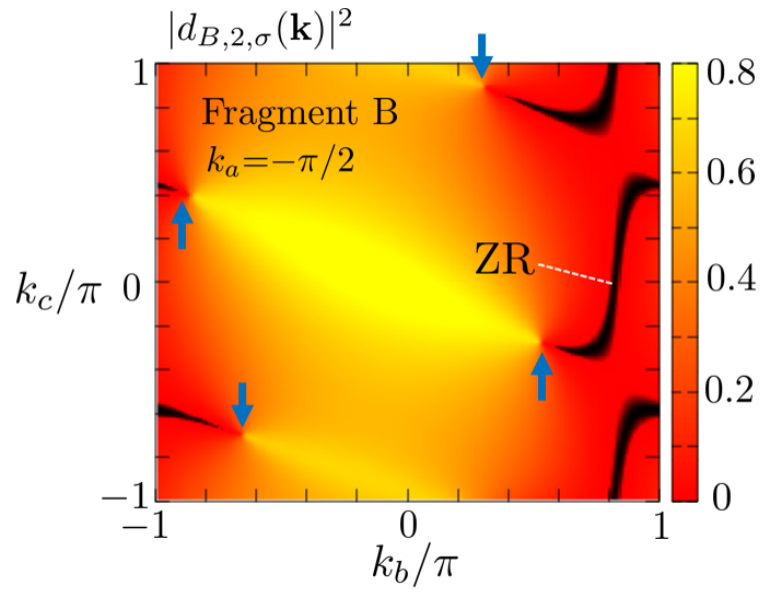


Figure 19: Squared absolute value of the wave function of orbital B in band 2, $|d_{B,2,\sigma}(\mathbf{k})|^2$, in the k_b - k_c plane, where $k_a = -\pi/2$. The up arrows stand for the positions of the Dirac points degenerated between the bands 1 and 2 in Fig. 17 (a), while the down arrows stand for those between the bands 2 and 3. The color bar shows the magnitude of $|d_{B,2,\sigma}(\mathbf{k})|^2$.

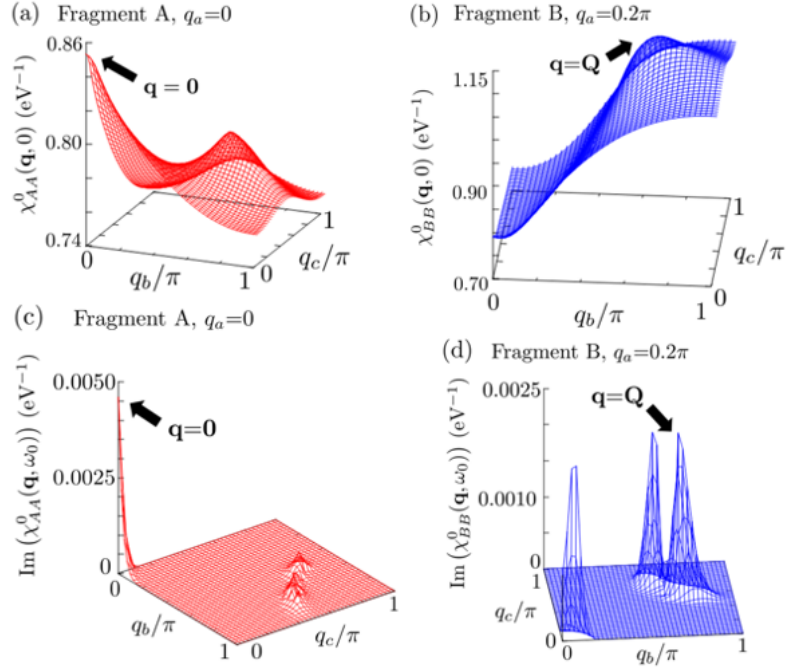


Figure 20: Momentum \mathbf{q} dependency of the diagonal elements of the spin susceptibility in the case of $U = 0$. (a) $\chi_{AA}^0(\mathbf{q}, 0)$ in the q_b - q_c plane, where $q_a=0$. (b) $\chi_{BB}^0(\mathbf{q}, 0)$ in the q_b - q_c plane, where $q_a=0.2\pi$. (c) $\text{Im}[\chi_{AA}^0(\mathbf{q}, \omega_0)]$ in the q_b - q_c plane, where $q_a=0$. (d) $\text{Im}[\chi_{BB}^0(\mathbf{q}, \omega_0)]$ in the q_b - q_c plane, where $q_a=0.2\pi$. The temperature is set to be $T=0.003$ eV.

momentum space is given by

$$\rho_\alpha(\mathbf{k}, \omega) = -\frac{1}{\pi} \text{Im} G_{\alpha\alpha}^{R,0}(\mathbf{k}, \omega), \quad (36)$$

where the spin index σ is omitted in Eq. 36. Eq. 36 at $\omega=0$ implies the spectral weight on the Fermi surface. $\rho_\alpha(\mathbf{k}, \omega)$ shows the weights of the respective fragment orbitals for the energy ω and the wavenumber \mathbf{k} because $G_{\alpha\alpha}^{R,0}(\mathbf{k}, \omega)$ in Eq. 36 includes the square of the absolute values of the wavefunctions $|d_{\alpha,n}(\mathbf{k})|^2$. In addition, the spectral weight and DOS have the relationship $\frac{1}{N_L} \sum_{\mathbf{k}} \rho_\alpha(\mathbf{k}, \omega) = D_\alpha(\omega)$. Figures 21 (a) and (b) show the spectral weights $\rho_A(\mathbf{k}, 0)$ and $\rho_B(\mathbf{k}, 0)$ in the k_b - k_c plane ($k_a=\pi$), respectively. In both figures, $-0.65\pi < k_b < -0.50\pi$ and $0.20\pi < k_c < 0.30\pi$. The orbital A does not have the momentum where its spectral weight becomes zero, but the spectral weight of B looks like a part of it lacks because orbital B has ZR in its wave function. This difference in spectral weights provides the spin susceptibilities with fragment-orbital dependence.

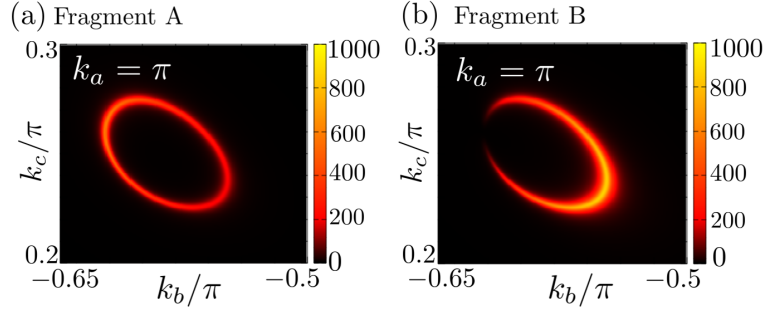


Figure 21: (a) Spectral weight $\rho_A(\mathbf{k}, 0)$, which is a finite value on any parts of the Fermi surface. (b) Spectral weight $\rho_B(\mathbf{k}, 0)$. ZR makes a part of it zero. In the both figures, $k_a=\pi$, $-0.65\pi < k_b < -0.50\pi$, and $0.20\pi < k_c < 0.30\pi$. Color bars show the magnitude of the spectral weights. The yellow region indicates momenta where the spectral weight on the Fermi surface is high.

After performing summation over the Matsubara frequency of the fermion $i\tilde{\omega}_m$ in Eq. 28, the non-interacting spin susceptibility is rewritten as

$$\begin{aligned} \chi_{\alpha,\beta}^0(\mathbf{q}, i\omega_l) = & -\frac{1}{N_L} \sum_{\mathbf{k}, m, n} \frac{f_{\mathbf{k}+\mathbf{q}, m} - f_{\mathbf{k}, n}}{\epsilon_{\mathbf{k}+\mathbf{q}, m} - \epsilon_{\mathbf{k}, n} - i\omega_l} \\ & \times d_{\alpha, m}(\mathbf{k} + \mathbf{q}) d_{\beta, m}^*(\mathbf{k} + \mathbf{q}) d_{\beta, n}(\mathbf{k}) d_{\alpha, n}^*(\mathbf{k}). \end{aligned} \quad (37)$$

I omit σ in Eq. 37. The terms in which the denominator and numerator are respectively close to 0 and 1 in Eq. 37 increase the non-interacting spin susceptibilities. Such terms are given by the wavenumber $\mathbf{k} + \mathbf{q}$ and \mathbf{k} near the Fermi surface. Thus, the vector \mathbf{q} connecting the Fermi surface,

which is called the nesting vector, greatly affects the spin susceptibility. The relationship between the nesting vector $\mathbf{q}=\mathbf{Q}$ and Fermi surface is shown in Fig. 22. $\mathbf{q}=\mathbf{Q}$ connects the momentum regions which give $\rho_B(\mathbf{k}, 0)$ high values. \mathbf{Q} provide the maximum value with $\chi_{BB}^0(\mathbf{q}, 0)$. Note that I do not calculation Eq. 37 but Eq. 28 using a fast Fourier transform.

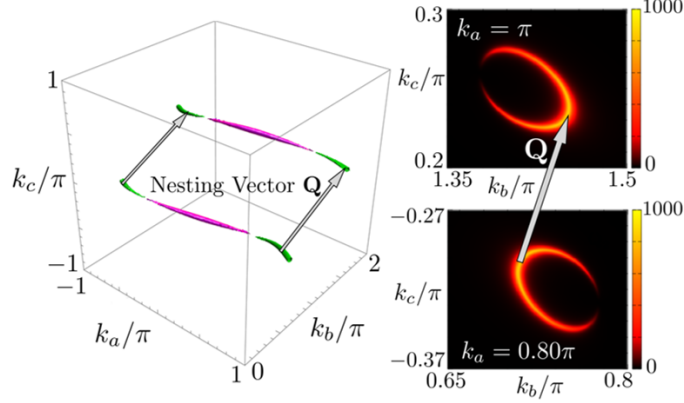


Figure 22: Nesting vector $\mathbf{q}=\mathbf{Q}$ is shown in the right figure. It connects the momentum regions which give $\rho_B(\mathbf{k}, 0)$ high values. The electron and hole pockets respectively are depicted in magenta and green.

I calculate the temperature dependence of $\chi_{\alpha\beta}^0(\mathbf{0}, 0)$ by solving Eq. 28 for $\mathbf{q}=\mathbf{0}$ because it is important to the following calculations. They have real values because $\mathbf{q}=\mathbf{0}$ and $\omega=0$. $\chi_{AA}^0(\mathbf{0}, 0)=\chi_{CC}^0(\mathbf{0}, 0)$, $\chi_{AB}^0(\mathbf{0}, 0)=\chi_{BC}^0(\mathbf{0}, 0)$ are satisfied because this material has the space-inversion symmetry. Behaviors of the spin susceptibilities $\hat{\chi}^0(\mathbf{0}, 0)$ are shown in Fig. 23. The diagonal element $\chi_{AA}^0(\mathbf{0}, 0)$ may look like almost constant, however, it slightly decreases with cooling. $\chi_{BB}^0(\mathbf{0}, 0)$ also slowly decreases with cooling. On the other hand, the off-diagonal elements $\chi_{AB}^0(\mathbf{0}, 0)$ and $\chi_{AC}^0(\mathbf{0}, 0)$ takes negative values and decrease with cooling. In order to show the terms determining the signs of $\chi_{AB}^0(\mathbf{0}, 0)$ and $\chi_{AC}^0(\mathbf{0}, 0)$, I define the band-resolved spin susceptibility (Eq. 38) and solve it.

$$\begin{aligned} \chi_{\alpha\beta, mn}^0(\mathbf{q}, i\omega_l) &= -\frac{T}{N_L} \sum_{\mathbf{k}, l'} G_{\alpha\beta, m}^0(\mathbf{k} + \mathbf{q}, i\tilde{\omega}_{l'} + i\omega_l) G_{\beta\alpha, n}^0(\mathbf{k}, i\tilde{\omega}_{l'}), \end{aligned} \quad (38)$$

$$G_{\alpha\beta, m, \sigma}^0(\mathbf{k}, i\tilde{\omega}_l) = d_{\alpha, m, \sigma}(\mathbf{k}) d_{\beta, m, \sigma}^*(\mathbf{k}) \frac{1}{i\tilde{\omega}_l - \epsilon_{\mathbf{k}, m, \sigma}}, \quad (39)$$

where m and n indicate the band indices. Eq. 38 satisfies $\sum_{m, n} \chi_{\alpha\beta, mn}^0(\mathbf{q}, i\omega_l) = \chi_{\alpha\beta}^0(\mathbf{q}, i\omega_l)$, where $\chi_{\alpha\beta}^0(\mathbf{q}, i\omega_l)$ is given by Eq. 28. In the inset of Fig. 23,

the temperature dependencies of $\chi_{AB,12}^0(\mathbf{0}, 0)$ and $\chi_{AC,12}^0(\mathbf{0}, 0)$ are shown. They take negative values and such terms give the off-diagonal elements of spin susceptibility, $\chi_{AB}^0(\mathbf{0}, 0)$ and $\chi_{AC}^0(\mathbf{0}, 0)$, negative signs.

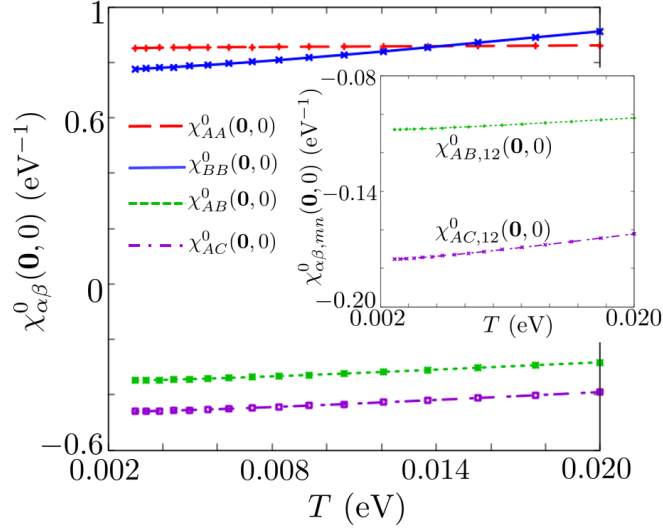


Figure 23: Behavior of $\chi_{\alpha\beta}^0(\mathbf{0}, 0)$. The red dashed, blue solid, green dotted, and purple chain lines show $\chi_{AA}^0(\mathbf{0}, 0)$, $\chi_{BB}^0(\mathbf{0}, 0)$, $\chi_{AB}^0(\mathbf{0}, 0)$, and $\chi_{AC}^0(\mathbf{0}, 0)$, respectively. The band-decided spin susceptibilities $\chi_{AB,12}^0(\mathbf{0}, 0)$ and $\chi_{AC,12}^0(\mathbf{0}, 0)$ are also depicted by the green dotted and purple chain lines, respectively.

I calculate the Knight shift in the case of $U = 0$ using Eq. 32. Knight shifts for the respective fragment orbitals are expressed by $K_A = \chi_{AA}^0(\mathbf{0}, 0) + \chi_{AB}^0(\mathbf{0}, 0) + \chi_{AC}^0(\mathbf{0}, 0)$ and $K_B = \chi_{BB}^0(\mathbf{0}, 0) + \chi_{BA}^0(\mathbf{0}, 0) + \chi_{BC}^0(\mathbf{0}, 0) = \chi_{BB}^0(\mathbf{0}, 0) + 2\chi_{BA}^0(\mathbf{0}, 0)$ by using the matrix elements of the spin susceptibilities, which are shown in Fig. 23, because of the space-inversion symmetry. The Knight shift for the fragment orbitals A and B is shown in Fig. 24. The Knight shift is dominated by the linear energy dispersion for temperatures higher than T^* . However, not only linear dispersion but also Fermi surface contribute to the Knight shift. The influence of the Fermi surface appears in $T \lesssim T^* \sim 0.01\text{eV}$. The Knight shift of the two-dimensional Dirac electron system for $U = 0$ is determined by $K_\alpha \simeq \int_{-\infty}^{\infty} D_\alpha(\omega) \left(-\frac{df(\omega)}{d\omega} \right) d\omega$. [113] $f(\omega)$ is the Fermi distribution function where the index ω is energy. K_α is proportional to T for $T \gtrsim T^*$ in Fig. 24 because local DOS is proportional to ω near the Fermi energy in Fig. 18. The Knight shift of the two-dimensional Dirac electron system becomes zero at $T=0$ because the DOS is zero at E_F . However, the K_α does not become proportional to T for $T \lesssim T^*$ because $D_\alpha(0)$ has a finite value (Fig. 18). This is the effect of the Fermi surface generated by the three-dimensional transfer integrals. The magnitude relationship $K_B > K_A$ is consistent with the one of $D_B(\omega) > D_A(\omega)$ near

E_F .

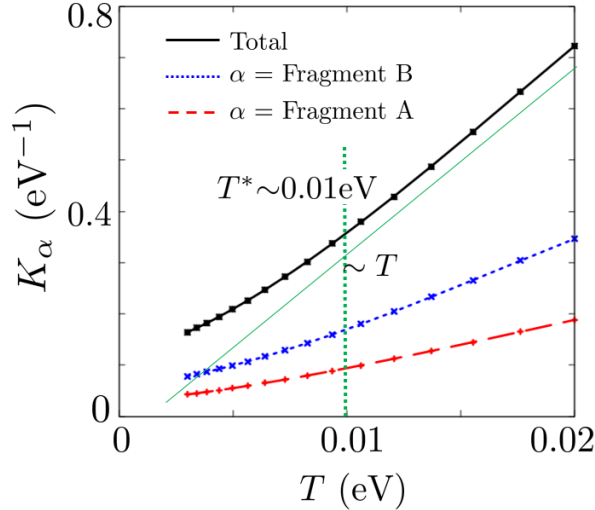


Figure 24: Behavior of K_α in the case of $U = 0$. The red dashed, blue dotted, black solid lines show K_A , K_B , and total Knight shift $K_{total}=K_A + K_B + K_C$, respectively. The green dotted longitudinal line represents $T=T^*\sim 0.01$ eV. The green thin line which is proportional to T is shown for the guiding eye.

Next, I calculate the spin-lattice relaxation rate $1/T_1T$ in the case of $U = 0$ using Eq. 33. $1/T_1T$ is determined by the imaginary part of the diagonal element of the spin susceptibility $\sum_{\mathbf{q}} \text{Im}[\chi_{\alpha\alpha}^0(\mathbf{q}, \omega_0)]$. Fig. 25 shows the temperature dependence of $1/T_1T$ in the case of $U = 0$. $(1/T_1T)_\alpha$ is proportional to T^2 for $T \gtrsim T^*$ in Fig. 24 because the $1/T_1T$ of the two-dimensional Dirac electron system is given by $(1/T_1T)_\alpha \simeq \int_{-\infty}^{\infty} [D_\alpha(\omega)]^2 \left(-\frac{df(\omega)}{d\omega}\right) d\omega$. It means that $\mathbf{q}=\mathbf{0}$ components of the imaginary parts of the spin susceptibilities contribute to $1/T_1T$. [113] $(1/T_1T)_\alpha$ is not proportional to T^2 for $T \lesssim T^*$ due to the Fermi surface.

3.3 Numerical result in the case of $U \neq 0$

I evaluate the Stoner factor, the Knight shift, and $1/T_1T$ in the case of $U \neq 0$. It is found that the enhancement of spin fluctuations by U is important for the behavior of the Knight shift and $1/T_1T$. [81, 82] According to Eq. 31, the Stoner factor $\xi_s(\mathbf{q})$ close to 1 is the main contributor for the spin susceptibility thus for the Knight shift and $1/T_1T$. $\xi_s(\mathbf{q} = \mathbf{0}) \approx 1$ contributes to the Knight shift and $1/T_1T$. $\xi_s(\mathbf{q} = \mathbf{Q}) \approx 1$ does not contribute to the Knight shift but to $1/T_1T$.

I calculate the Stoner factor $\xi_s(\mathbf{q})$ because it takes on an important role in enhancement of spin fluctuations. Figure 26 shows the behavior of $\xi_s(\mathbf{q})$,

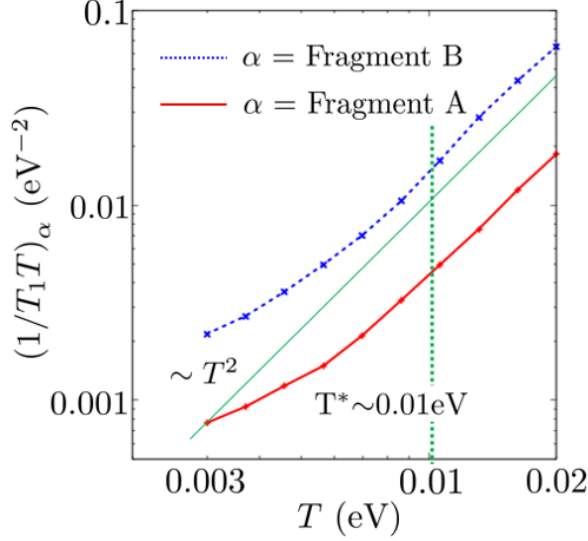


Figure 25: Behavior of $(1/T_1 T)_\alpha$ in the case of $U = 0$. The A and B components, $(1/T_1 T)_A$ and $(1/T_1 T)_B$, are shown red solid and blue dotted lines, respectively. The dashed longitudinal line represents $T=T^* \sim 0.01$ eV. The green thin line which is proportional to T^2 is drawn for guiding eyes.

where the horizontal axis represents T . I set $U=0.802$ and $\lambda=0.95$. The value $\lambda=0.95$ is acquired at the time of estimating the screened Coulomb repulsion by RESPACK. $\xi_s(\mathbf{q})$ value is maximum at $\mathbf{q}=\mathbf{0}$ and increases with cooling. The parameters $\lambda=0.95$ and $U=0.802$ provide $\xi_s(\mathbf{0})=0.999$ at $T=0.003$ eV. Meanwhile, $\xi_s(\mathbf{Q})$ slowly decreases with cooling and $\xi_s(\mathbf{Q}) < \xi_s(\mathbf{0})$ then. \mathbf{Q} is the wavenumber where $\chi_{BB}^0(\mathbf{q}, 0)$ and $\chi_{BB}^0(\mathbf{q}, 0)$ are maximum in the momentum space. $\xi_s(\mathbf{0}) > \xi_s(\mathbf{Q})$ shows that the $\mathbf{q}=\mathbf{0}$ magnetic order is easily induced than incommensurate SDW.

I explain reason why $\xi_s(\mathbf{0})$ increases with cooling. in the case of $U \neq 0$, $\xi_s(\mathbf{q})$ isn't directly determined by the DOS because the maximum eigenvalue of $\hat{U}\hat{\chi}^0(\mathbf{q}, 0)$ includes the products of the $\chi_{\alpha\beta}^0(\mathbf{q}, 0)$. It means that the Coulomb interaction is essential for the spin fluctuations. I calculate the first- and second-order perturbation terms in Eq. (A) and (B) in Fig. 16. Eq. (A) and (B) in Fig. 16 are equivalent because the SOC is not considered and external fields are imposed. Their matrix elements $\chi_{\alpha\beta}^{s,1st}(\mathbf{q}, i\omega_l)$ and $\chi_{\alpha\beta}^{s,2nd}(\mathbf{q}, i\omega_l)$ are expressed by

$$\chi_{\alpha\beta}^{s,1st}(\mathbf{q}, i\omega_l) = \sum_{\gamma} \chi_{\alpha\gamma}^0(\mathbf{q}, i\omega_l) U_{\gamma\gamma} \chi_{\gamma\beta}^0(\mathbf{q}, i\omega_l), \quad (40)$$

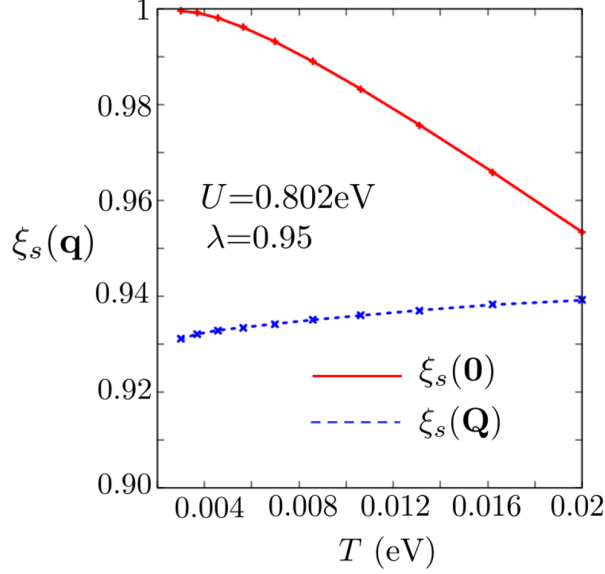


Figure 26: $\xi_s(\mathbf{0})$ and $\xi_s(\mathbf{Q})$ are shown as functions of T by the red solid and blue dotted lines, respectively.

$$\begin{aligned} \chi_{\alpha\beta}^{s,2nd}(\mathbf{q}, i\omega_l) &= \sum_{\gamma, \gamma'} \chi_{\alpha\gamma}^0(\mathbf{q}, i\omega_l) U_{\gamma\gamma} \chi_{\gamma\gamma'}^0(\mathbf{q}, i\omega_l) \\ &\times U_{\gamma'\gamma'} \chi_{\gamma'\beta}^0(\mathbf{q}, i\omega_l). \end{aligned} \quad (41)$$

They are the first- and second-order perturbation terms in RPA and correspond to the second and third terms in the right-hand of Eq. (A) or (B) in Fig. 16, respectively. Figure 27 shows the temperature dependence of $\chi_{AA}^{s,1st}(\mathbf{0}, 0)$ and $\chi_{AA}^{s,2nd}(\mathbf{0}, 0)$. They increase as with cooling. Because the off-diagonal elements of $\hat{\chi}^0(\mathbf{0}, 0)$ are negative and decrease with cooling in Fig. 23, their squares of absolute values increase. Thus, terms such as $\chi_{AB}^0(\mathbf{0}, 0)U_{BB}\chi_{BA}^0(\mathbf{0}, 0)$ in Eq. 40 and $\chi_{AC}^0(\mathbf{0}, 0)U_{CC}\chi_{CC}^0(\mathbf{0}, 0)U_{CC}\chi_{CA}^0(\mathbf{0}, 0)$ in Eq. 41 increase $\chi_{AA}^{s,1st}(\mathbf{0}, 0)$ and $\chi_{AA}^{s,2nd}(\mathbf{0}, 0)$ with cooling. The other higher-order perturbation terms have similar temperature dependencies. Thus, $\xi_s(\mathbf{0})$ has the large value in low T .

Fragment orbitals A and C are sensitive to $\xi_s(\mathbf{0})$ while fragment orbital B is sensitive to $\xi_s(\mathbf{Q})$. I determine the matrix elements of $\hat{\chi}^s(\mathbf{0}, 0)$ and $\hat{\chi}^s(\mathbf{Q}, 0)$ to show these behaviors by solving Eqs. 28 and 30. Temperature dependence of $\chi_{AA}^s(\mathbf{0}, 0)$, $\chi_{BB}^s(\mathbf{0}, 0)$, $\chi_{AB}^s(\mathbf{0}, 0)$, and $\chi_{AC}^s(\mathbf{0}, 0)$ are shown in Fig. 28(a). They have the real values because $\mathbf{q}=0$ and $i\omega_l=0$. $\chi_{AA}^s(\mathbf{0}, 0)=\chi_{CC}^s(\mathbf{0}, 0)$, $\chi_{AB}^s(\mathbf{0}, 0)=\chi_{BA}^s(\mathbf{0}, 0)=\chi_{BC}^s(\mathbf{0}, 0)=\chi_{CB}^s(\mathbf{0}, 0)$, and $\chi_{AC}^s(\mathbf{0}, 0)=\chi_{CA}^s(\mathbf{0}, 0)$ are satisfied due to space-inversion symmetry. The inset is the enlarged figure around $\chi_{BB}^s(\mathbf{0}, 0)$ and $\chi_{AB}^s(\mathbf{0}, 0)$. $\chi_{BB}^s(\mathbf{0}, 0)$ and $\chi_{AB}^s(\mathbf{0}, 0)$ do not increase at low T , while $\chi_{AA}^s(\mathbf{0}, 0)$ sharply increases. In addition, $\chi_{AC}^s(\mathbf{0}, 0)$ sharply decreases with cooling and takes the negative

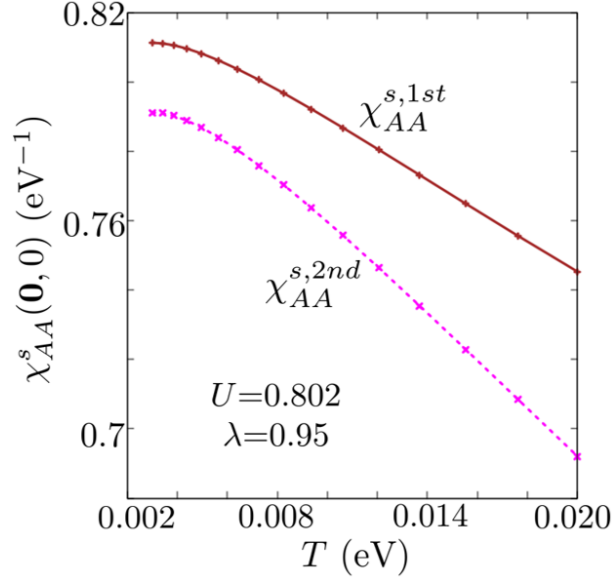


Figure 27: Behavior of first- and second-order perturbation terms of $\chi_{AA}^s(\mathbf{0}, 0)$ are shown by the brown solid and magenta dotted line, respectively.

value. $\xi_s(\mathbf{0})$ greatly contributes to the orbitals A and C but not the orbital B. The negative $\chi_{AC}^s(\mathbf{0}, 0)$ implies that intra-molecular antiferromagnetic fluctuations are enhanced. The negative off-diagonal elements of the interacting spin susceptibility result from the distinctive wave functions of the Dirac nodal line system.

Figure 28(b) shows the behaviors of $\text{Re}[\chi_{AA}^s(\mathbf{Q}, 0)]$, $\text{Re}[\chi_{BB}^s(\mathbf{Q}, 0)]$, $\text{Re}[\chi_{AB}^s(\mathbf{Q}, 0)]$, and $\text{Re}[\chi_{AC}^s(\mathbf{Q}, 0)]$. $\text{Re}[\hat{\chi}^s(\mathbf{Q}, 0)]$ link to $\xi_s(\mathbf{Q})$ and slowly varies with T . $\text{Re}[\chi_{BB}^s(\mathbf{Q}, 0)]$ is the largest of all matrix elements and slowly increases with T . Fragment orbital B is influenced by $\xi_s(\mathbf{Q})$. The spin correlation between the fragment orbitals B and A(C) within a molecule is antiparallel because $\text{Re}[\chi_{AB}^s(\mathbf{Q}, 0)]$ is negative and $\text{Re}[\chi_{AC}^s(\mathbf{Q}, 0)]$ is positive.

Figure 29 shows a schematic of the spin fluctuations within a molecule. Figure 29 (a) illustrates the case in Fig. 28 (a), where the intra-molecular antiferromagnetic spin fluctuations appears. The solid arrows in Fig. 29 (a) illustrate that an infinitesimal downward local magnetic field on the orbital C(A) gives the orbital A(C) an upward spin polarization by the linear response relation $M_{A(C)} = \chi_{AC(CA)}^s \Delta H_{C(A)}$, respectively, where M and ΔH are magnetization and infinitesimal magnetic field. Figure 29(b), which is derived from Fig. 28(b), illustrates the spin fluctuations within a molecule that are incommensurate ($\mathbf{q} \neq \mathbf{Q}$) between molecules. In the case of the $\mathbf{q} = \mathbf{Q}$ spin fluctuations, the spins at the orbitals A(=C) and B are apt to be inversely correlated within a molecule.

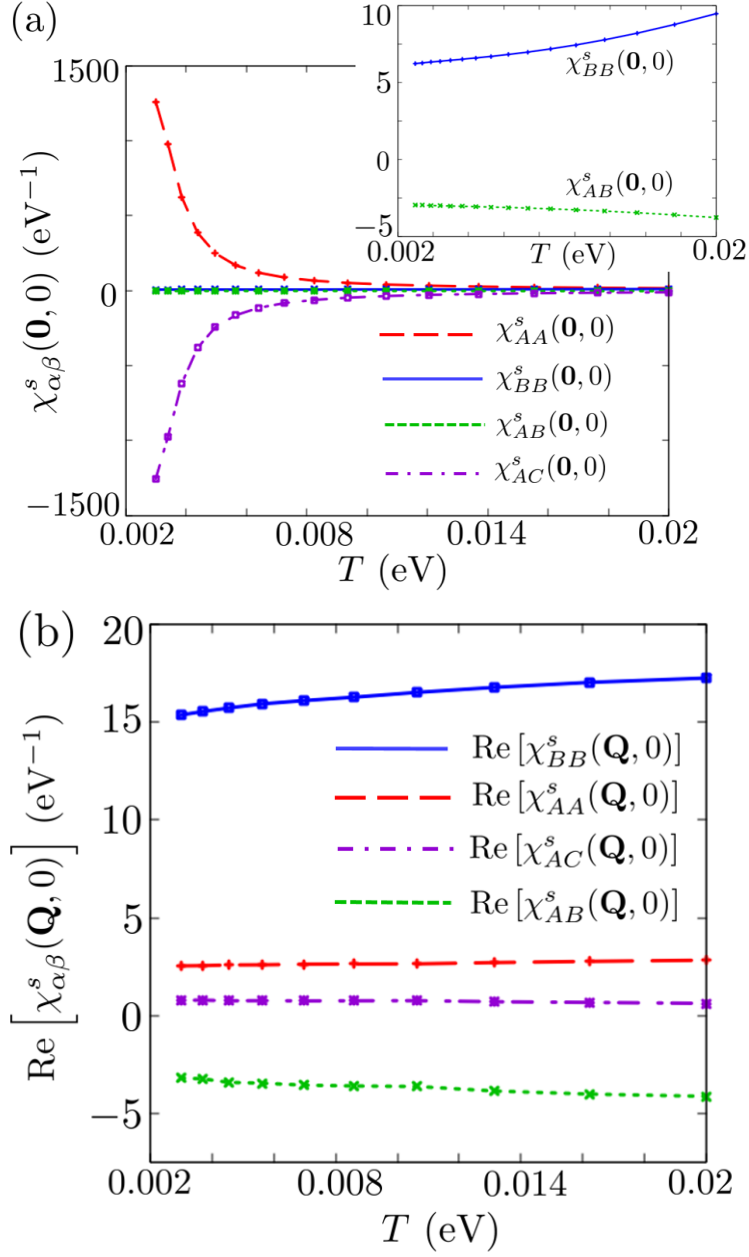


Figure 28: (a) Behaviors of $\chi_{AA}^s(\mathbf{0}, 0)$, $\chi_{BB}^s(\mathbf{0}, 0)$, $\chi_{AB}^s(\mathbf{0}, 0)$, and $\chi_{AC}^s(\mathbf{0}, 0)$ are shown by the red dashed, blue solid, green dotted, and purple chain lines, respectively. The inset shows an enlarged view of the region around $\chi_{BB}^s(\mathbf{0}, 0)$ and $\chi_{AB}^s(\mathbf{0}, 0)$. (b) Behaviors of $\text{Re}[\chi_{AA}^s(\mathbf{Q}, 0)]$, $\text{Re}[\chi_{BB}^s(\mathbf{Q}, 0)]$, $\text{Re}[\chi_{AB}^s(\mathbf{Q}, 0)]$, and $\text{Re}[\chi_{AC}^s(\mathbf{Q}, 0)]$. The combination of matrix elements and lines is the same as in (a).

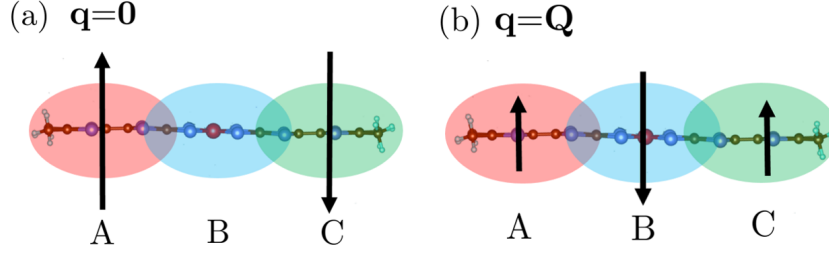


Figure 29: Spin correlation within a molecule is schematically depicted. (a) Intra-molecular antiferromagnetic spin fluctuations, which correspond to $\mathbf{q}=\mathbf{0}$ response, are shown in Fig. 28(a). (b) Spin correlation within a molecule given by the $\mathbf{q}=\mathbf{Q}$ response in Fig. 28(b).

Next, I show $\chi_{\alpha\alpha}^s(\mathbf{q}, \omega)$ at $T=0.003$ eV. Figure 30 (a), (b), (c), and (d) show $\chi_{AA}^s(\mathbf{q}, 0)$, $\chi_{BB}^s(\mathbf{q}, 0)$, $\text{Im}[\chi_{AA}^s(\mathbf{q}, \omega_0)]$, and $\text{Im}[\chi_{BB}^s(\mathbf{q}, \omega_0)]$ in the q_b - q_c plane, respectively. $\chi_{\alpha\alpha}^s(\mathbf{q}, 0)$ has the real value. I fix $q_a=0$ in Fig. 30 (a) and (c) and $q_a=0.2\pi$ in Fig. 30 (b) and (d). The real frequency ω_0 is set to be 0.001 eV. $\chi_{AA}^s(\mathbf{q}, 0)$ and $\text{Im}[\chi_{AA}^s(\mathbf{q}, \omega_0)]$ have very large values at $\mathbf{q}=\mathbf{0}$ because the Stoner factor is almost 1 ($\xi_s(\mathbf{0})=0.999$). However, the BB component is insensitive to $\xi_s(\mathbf{0})$ but sensitive to $\xi_s(\mathbf{Q})$. \mathbf{Q} is the wavenumber where $\chi_{BB}^0(\mathbf{q}, 0)$ and $\chi_{BB}^s(\mathbf{q}, 0)$ become maximum. $\chi_{AA}^s(\mathbf{0}, 0)$ and $\text{Im}[\chi_{AA}^s(\mathbf{0}, \omega_0)]$ are much larger than $\chi_{BB}^s(\mathbf{Q}, 0)$ and $\text{Im}[\chi_{BB}^s(\mathbf{Q}, \omega_0)]$ because $\xi_s(\mathbf{0}) > \xi_s(\mathbf{Q})$ and the spin susceptibility obtained by RPA is dominated by $1/(1 - \xi_s(\mathbf{q}))$. $\chi_{AA}^s(\mathbf{0}, 0)$ and $\text{Im}[\chi_{AA}^s(\mathbf{0}, \omega_0)]$ in Fig. 30 (a) and (c) decrease with temperature. Whereas, $\chi_{BB}^s(\mathbf{Q}, 0)$ and $\text{Im}[\chi_{BB}^s(\mathbf{Q}, \omega_0)]$ in Fig. 30 (b) and (d) increase and width of the peaks become very broad with temperature. These are caused by the behavior of $\xi_s(\mathbf{q})$ in Fig. 26 and the fragment-orbital dependent spin fluctuations.

I calculate Eq. 32 and 33 to investigate the influence of the spin fluctuations on the Knight shift and $1/T_1T$, which are physical quantities observed by ^{13}C -NMR experiment.

Fig. 31 shows the Knight shift where $U=0.802$ and $\lambda=0.95$. The horizontal axis indicates temperature. K_B in the case of $U \neq 0$ is larger than that in the case of $U = 0$. On the other hand, K_A and K_C in the case of $U \neq 0$ are smaller than those in the case of $U = 0$ and have negative values. On the other hand, K_B and $K_{tot}(=K_A + K_B + K_C)$ have positive values. Similar behavior was proposed in the previous research about the organic conductor α -(BEDT-TTF) $_2\text{I}_3$, which is the two-dimensional Dirac electron system.[51]

Although the Stoner factor $\xi_s(\mathbf{0})$ is almost 1 at $T=0.003$ eV, K_A and K_C monotonically decrease with cooling. The mechanism of this behavior is unraveled by analyzing the off-diagonal elements of $\hat{\chi}^s(\mathbf{0}, 0)$. Because $\chi_{AA}^s(\mathbf{0}, 0)$ and $\chi_{AC}^s(\mathbf{0}, 0)$ have opposite signs in Fig. 28(a), their cancellation prevents the Knight shift from increasing in Eq. 32. Thus, the $\mathbf{q}=\mathbf{0}$

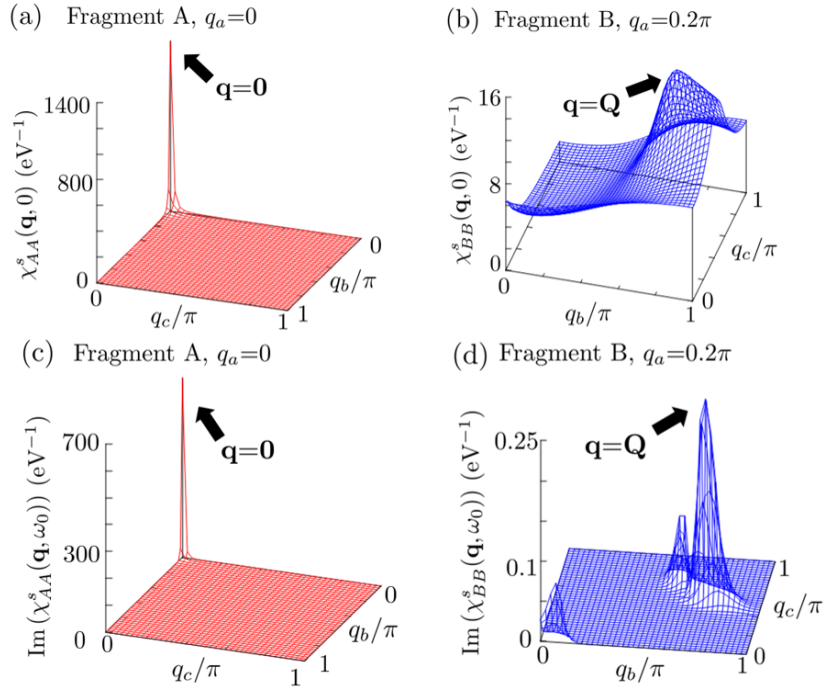


Figure 30: The diagonal elements of the spin susceptibility in q_b - q_c plane. (a) $\chi_{AA}^s(\mathbf{q}, 0)$ in the q_b - q_c plane, where $q_a=0$. (b) $\chi_{BB}^s(\mathbf{q}, 0)$ in the q_b - q_c plane, where $q_a=0.2\pi$. (c) $\text{Im}[\chi_{AA}^s(\mathbf{q}, \omega_0)]$ in the q_b - q_c plane, where $q_a=0$. (d) $\text{Im}[\chi_{BB}^s(\mathbf{q}, \omega_0)]$ in the q_b - q_c plane, where $q_a=0.2\pi$.

spin fluctuations do not appear in the Knight shift because it is the intra-molecular antiferromagnetic fluctuations.

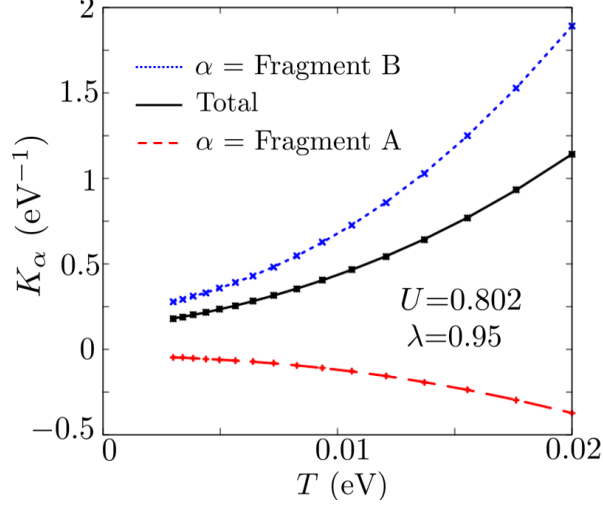


Figure 31: Behavior of K_α where $U=0.802$ and $\lambda=0.95$. K_A , K_B , and $K_{\text{tot}}(=K_A+K_B+K_C)$ are depicted by the red dashed, blue dotted, and black solid lines, respectively.

Next, I calculate Eq. 33. $1/T_1T$, which is determined by $\sum_{\mathbf{q}} \text{Im}[\chi_{\alpha\alpha}^s(\mathbf{q}, \omega_0)]$, is shown in Fig. 32 ($\lambda=0.95$, $U=0.802$). The horizontal axis indicates temperature. At high T , $1/T_1T$ values for all fragment orbitals decrease with cooling, however, the $(1/T_1T)_A(=(1/T_1T)_C)$ starts to increase in low T because fragment A is greatly contributed by $\xi_s(\mathbf{0})$. On the other hand, $(1/T_1T)_B$ does not increase because orbital B is insensitive to $\xi_s(\mathbf{0})$. For $T \gtrsim 0.005$ eV, $(1/T_1T)_B$ become larger than $(1/T_1T)_A$ and $(1/T_1T)_C$. Not only $\mathbf{q}=\mathbf{0}$ component but also $\mathbf{q} \sim \mathbf{Q}$ component contribute to $(1/T_1T)_B$ because the peak $\text{Im}[\chi_{BB}^S(\mathbf{Q}, \omega_0)]$ become broad and $\xi_s(\mathbf{Q})$ slowly increases with T . $(1/T_1T)_A$ and $(1/T_1T)_C$ doesn't become as large as $(1/T_1T)_B$ because they are difficult to be affected by $\xi(\mathbf{Q})$.

In the case of a small λ , $\xi_s(\mathbf{Q})$ is larger than $\xi_s(\mathbf{0})$, and SDW can be induced. However, the Stoner factor $\xi_s(\mathbf{Q})$ is suppressed at low T as shown in Fig. 26. Thus, incommensurate spin fluctuations do not reproduce the upturn of the $1/T_1T$ curve near 30 K. I estimate λ using RESPACK in this study. $\lambda=0.79$ and $\lambda=0.95$ are obtained as the ratios of diagonal elements with the unscreened and screened on-site Coulomb interactions, respectively. Therefore, I consider that $\lambda=0.95$ is more realistic than $\lambda=0.79$.

In this subsection, I showed that the Knight shift monotonically decreases with cooling due to the intra-molecular antiferromagnetic fluctuations. I also showed that the $(1/T_1T)_A$ and $(1/T_1T)_C$ start to increase at low T due to the behavior of Stoner factor $\xi_s(\mathbf{0})$. They are dominant in

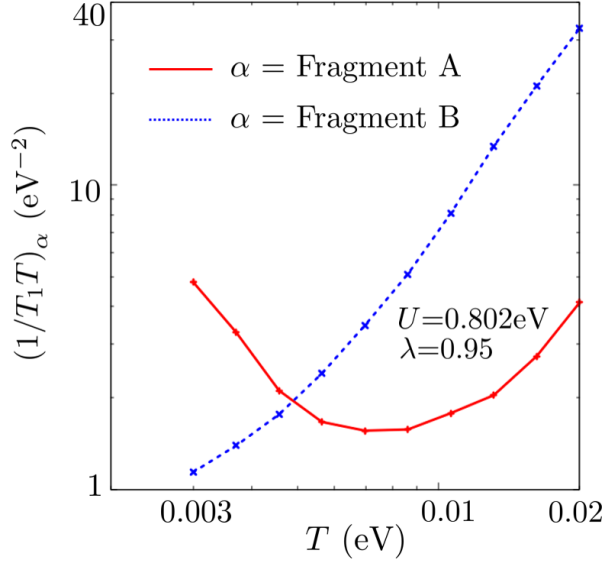


Figure 32: Behavior of $(1/T_1 T)_\alpha$ where $U=0.802$ and $\lambda=0.95$. The red solid and blue dotted lines show $(1/T_1 T)_A$ and $(1/T_1 T)_B$, respectively.

$T \lesssim 0.005$ eV, while $(1/T_1 T)_B$ become larger than $(1/T_1 T)_A$ and $(1/T_1 T)_C$ in $T \gtrsim 0.005$ eV because of behavior of $\xi_s(\mathbf{Q})$ and fragment-orbital-dependence of spin fluctuations. Fig. 33 summarizes the fragment-orbital dependence of the Fermi surface, non-interacting spin susceptibilities, Stoner factors, and $1/T_1 T$. Fig. 33 shows the important factors for orbitals A and B. $\xi_s(\mathbf{0})$ mainly contributes to orbital A and gives $(1/T_1 T)_A$ large value at low T . However, Orbital B is insensitive to $\xi_s(\mathbf{0})$ but sensitive to $\xi_s(\mathbf{Q})$, which contributes to $(1/T_1 T)_B$ at high T . The contribution of $\xi_s(\mathbf{Q})$ to orbital A and C is small. These fragment-orbital-dependent spin fluctuations result from the ZR in the momentum space because the spectral weight $\rho_B(\mathbf{k}, 0)$ in Eq. 36 is biased to a part of the Fermi surface.

3.4 Summary and discussion

It is found that the idea of fragment orbitals is significant in investigating the spin fluctuations and the physical quantities related to the NMR experiment in $[\text{Ni}(\text{dmdt})_2]$. For fragments A and C, which are localized on one side of the molecule, the commensurate spin fluctuations ($\mathbf{q}=\mathbf{0}$) are enhanced, while the incommensurate spin fluctuations are enhanced in fragment B, which is localized at the center of the molecule. The $\mathbf{q}=\mathbf{0}$ spin fluctuations make $(1/T_1 T)_A$ and $(1/T_1 T)_C$ increase with cooling at low T . However, they don't appear in the Knight shift due to the intramolecular antiferromagnetic fluctuations. The mechanism of enhancement of the $\mathbf{q}=\mathbf{0}$ spin fluctuations is understood from the scattering process in RPA and behavior


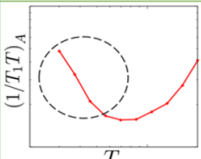

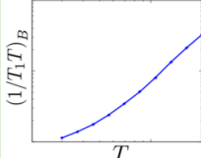
Orbital α	Fermi surface	$\chi_{\alpha\alpha}^0(\mathbf{q}, 0)$	$\xi_s(\mathbf{q})$	$(1/T_1T)_\alpha$
$\alpha=A$		Maximum value at $\mathbf{q} = \mathbf{0}$	$\xi_s(\mathbf{0})$	
$\alpha=B$		Maximum value at $\mathbf{q} = \mathbf{Q}$	$\xi_s(\mathbf{Q})$	

Figure 33: Table summarizing the Fermi surface, \mathbf{q} giving $\chi_{\alpha\alpha}^0(\mathbf{q}, 0)$ peaks, Stoner factors, and $1/T_1T$ for the orbitals A and B.

of $\hat{\chi}^0(\mathbf{0}, 0)$. On the other hand, the incommensurate spin fluctuations make $(1/T_1T)_B$ large in $T \gtrsim 0.005$ eV. These fragment-orbital-dependent physical quantities result from the ZR. If there is no ZR in the momentum space, it is considered that the B diagonal element of the spin susceptibilities is not maximum at the incommensurate wavenumber, because the behaviors of the spectral weight $\rho_\alpha(\mathbf{k}, 0)$ for all fragments may be similar. Because $\rho_B(\mathbf{k}, 0)$ in Eq. 36 is significantly biased on the part of the Fermi surface due to the existence of ZR, the B diagonal element of the spin susceptibility becomes maximum at the incommensurate wavenumber. Therefore, the behaviors of the spin susceptibilities in the momentum space are different depending on the fragments. The fragment-orbital-dependent behaviors of physical quantities are expected to be found in other Dirac nodal line systems because ZR is a character of the Dirac nodal line system expressed by an n -band low energy effective model ($n \geq 3$). In addition, it is predicted that tuning U and λ by transition-metal substitution controls spin fluctuations appearing in the observable quantities. In the two-dimensional Dirac electron system under the charge-neutral condition, the spin fluctuations may be weak because it has no transfer integral creating a Fermi surface. Whereas, not only intramolecular antiferromagnetic fluctuations but also incommensurate spin fluctuations are enhanced in $[\text{Ni}(\text{dmdt})_2]$ because the hopping in the nodal line direction makes the Fermi surface. This is the three-dimensionality of $[\text{Ni}(\text{dmdt})_2]$.

^{13}C -NMR experiments reported that $1/T_1T$ has a peak structure at $T \sim 30\text{K}$. This experiment was performed on a sample in which ^{12}C atoms were replaced by ^{13}C . In Figure 14 (b), the ^{13}C atom is surrounded by a red dotted circle. Thus, the A and C orbitals are the main contributors to the physical quantities measured in the ^{13}C -NMR experiments. Therefore, the numerical results of $1/T_1T$ obtained in this study are considered to be in qualitative agreement with the experimental results. Furthermore, the

behavior of $(1/T_1T)_B$ is expected to appear remarkably in the experiment using a sample in which ^{12}C atoms near the Ni atoms are replaced by ^{13}C . On the other hand, the Knight shifts of the A and C orbitals are negative in the numerical calculations, while the Knight shifts observed in the ^{13}C -NMR experiments are positive at any temperature. Therefore, I consider the following electronic state possibilities in $T \lesssim 30$ K. The first possibility is that the intramolecular antiferromagnetic order is stabilized at $T \lesssim 30$ K, and the experimental Knight shift measures the sum of K_A and K_B . In the second possibility, U is not large enough to make K_A negative. Next, I consider that another order stabilizes at $T \lesssim 30$ K and that the fluctuations corresponding to that order increase $(1/T_1T)$ with cooling.

4 Conclusion

In this paper, I investigated the magnetic properties of the organic conductors $(\text{EDO-TTF-I})_2\text{ClO}_4$ and $[\text{Ni}(\text{dmdt})_2]$, focusing on the molecular orbital degrees of freedom. The former is the inequivalent dimers and the latter is the fragment orbitals. In the work on $(\text{EDO-TTF-I})_2\text{ClO}_4$, I found that the antiferromagnetic order of the dimer is induced by electron correlation effects and that the inequivalence of the dimer leads to giant spin splitting. Since the charge gap is finite ($\Delta_C \sim 0.4$ eV), the ground state of this material is a compensated ferrimagnetic insulator. If the energy gap is controlled by pressure or temperature, a compensated ferrimagnetic semimetal can be made in the system. Thus, the inequivalent dimer system is expected to be useful for the generation of spin currents. In the study of $[\text{Ni}(\text{dmdt})_2]$, it was found that the spin fluctuations depend on the intramolecular fragment orbitals. Two types of intramolecular antiferromagnetic fluctuations ($\mathbf{q}=\mathbf{0}$) and incommensurate spin fluctuations ($\mathbf{q}=\mathbf{Q}$) are obtained. The fragment dependence of the spin fluctuations is attributed to the wave function of the Dirac nodal line system. These studies show that the degrees of freedom of molecular orbitals are an important key to calculating physical quantities related to the novel magnetism.

Acknowledgements

I would like to express my gratitude to Akito Kobayashi, K. Yoshimi, T. Misawa, and K. Hashimoto for their careful guidance in writing this thesis. I also thank to T. Sekine, T. Hatamura, K. Sunami, K. Miyagawa, K. Kanoda, B. Zhou, Akiko Kobayashi, Y. Nakano, and Sc laboratory members for fruitful discussions.

References

- [1] L. Šmejkal, A. H. MacDonald, J. Sinova, S. Nakatsuji, and T. Jungwirth, *Nat. Rev. Mater.* **7**, 482 (2022).
- [2] L. Šmejkal, J. Sinova, and T. Jungwirth, *Phys. Rev. X* **12**, 031042 (2022).
- [3] L. Šmejkal, J. Sinova, and T. Jungwirth, *Phys. Rev. X* **12**, 040501 (2022).
- [4] I. Mazin (The PRX Editors), *Phys. Rev. X* **12**, 040002 (2022).
- [5] Y. Noda, K. Ohno, and S. Nakamura, *Physical Chemistry Chemical Physics* **18**, 13294 (2016).

- [6] M. Naka, S. Hayami, H. Kusunose, Y. Yanagi, Y. Motome, and H. Seo, *Nat. Commun.* **10**, 1 (2019).
- [7] S. Hayami, Y. Yanagi, and H. Kusunose, *J. Phys. Soc. Jpn.* **88**, 123702 (2019).
- [8] K.-H. Ahn, A. Hariki, K.-W. Lee, and J. Kuneš, *Phys. Rev. B* **99**, 184432 (2019).
- [9] L.-D. Yuan, Z. Wang, J.-W. Luo, E. I. Rashba, and A. Zunger, *Phys. Rev. B* **102**, 014422 (2020).
- [10] L. Šmejkal, R. González-Hernández, T. Jungwirth, and J. Sinova, *Sci. Adv.* **6**, eaaz8809 (2020).
- [11] I. I. Mazin, K. Koepernik, M. D. Johannes, R. González-Hernández, and L. Šmejkal, *Proc. Natl. Acad. Sci.* **118**, e2108924118 (2021).
- [12] Z. Feng, X. Zhou, L. Šmejkal, L. Wu, Z. Zhu, H. Guo, R. González-Hernández, X. Wang, H. Yan, P. Qin, et al., *Nat. Electron.* **5**, 735 (2022).
- [13] H. van Leuken and R. A. de Groot, *Phys. Rev. Lett.* **74**, 1171 (1995).
- [14] W. E. Pickett, *Phys. Rev. B* **57**, 10613 (1998).
- [15] H. Akai and M. Ogura, *Phys. Rev. Lett.* **97**, 026401(2006).
- [16] S. A. Egorov and R. A. Evarestov, *J. Phys. Chem. Lett.* **12**, 2363 (2021).
- [17] R. Stinshoff, G. H. Fecher, S. Chadov, A. K. Nayak, B. Balke, S. Ouardi, T. Nakamura, and C. Felser, *AIP Adv.* **7**, 105009 (2017).
- [18] R. Stinshoff, A. K. Nayak, G. H. Fecher, B. Balke, S. Ouardi, Y. Skourski, T. Nakamura, and C. Felser, *Phys. Rev. B* **95**, 060410 (2017).
- [19] P. Midhunlal, J. A. Chelvane, D. Prabhu, R. Gopalan, and N. H. Kumar, *J. Magn. Mater.* **489**, 165298 (2019).
- [20] S. Semboshi, R. Y. Umetsu, Y. Kawahito, and H. Akai, *Sci. Rep.* **12**, 10687 (2022).
- [21] Y. Nakano, Y. Takahashi, K. Ishida, M. Ishikawa, and H. Yamochi, Private Communication.
- [22] T. Ando, T. Nakanishi, and R. Saito, *J. Phys. Soc. Jpn.* **67**, 2857 (1998).
- [23] V. P. Gusynin and S. G. Sharapov, *Phys. Rev. B* **73**, 245411 (2006).
- [24] S. Murakami, N. Nagaosa, and S.-C. Zhang, *Phys. Rev. Lett.* **93**, 156804 (2004).
- [25] D. Hsieh, D. Qian, L. Wray, Y. Xia, Y. S. Hor, R. J. Cava, and M. Z. Hasan, *Nature* **452**, 970–974 (2008).
- [26] H. Fukuyama and R. Kubo, *J. Phys. Soc. Jpn.* **28**, 570 (1970).

- [27] H. Fukuyama, J. Phys. Soc. Jpn. **76**, 043711 (2007).
- [28] A. A. Abrikosov and S. D. Beneslavskii, Zh. Eksp. Teor. Fiz. **59**, 1280 (1971).
- [29] J. González, F. Guinea, and M. A. H. Vozmediano, Nucl. Phys., Sect. B **424**, 595 (1994).
- [30] J. González, F. Guinea, and M. A. H. Vozmediano, Phys. Rev. B **59**, R2474(R) (1999).
- [31] V. N. Kotov, B. Uchoa, V. M. Pereira, F. Guinea, and A. H. Castro Neto, Rev. Mod. Phys. **84**, 1067 (2012).
- [32] T. O. Wehling, A. M. Black-Schaffer, and A. V. Balatsky, Adv. Phys. **63**, 1 (2014).
- [33] W. Witczak-Krempa, G. Chen, Y. B. Kim, and L. Balents, Annu. Rev. Condens. Matter Phys. **5**, 57 (2014).
- [34] K. Kajita, T. Ojiro, H. Fujii, Y. Nishio, H. Kobayashi, A. Kobayashi, and R. Kato, J. Phys. Soc. Jpn. **61**, 23 (1992).
- [35] N. Tajima, M. Tamura, Y. Nishio, K. Kajita, and Y. Iye, J. Phys. Soc. Jpn. **69**, 543 (2000).
- [36] A. Kobayashi, S. Katayama, K. Noguchi, and Y. Suzumura, J. Phys. Soc. Jpn. **73**, 3135 (2004).
- [37] S. Katayama, A. Kobayashi, and Y. Suzumura, J. Phys. Soc. Jpn. **75**, 054705 (2006).
- [38] A. Kobayashi, S. Katayama, Y. Suzumura, and H. Fukuyama, J. Phys. Soc. Jpn. **76**, 034711 (2007).
- [39] M. O. Goerbig, J. N. Fuchs, G. Montambaux, and F. Piéchon, Phys. Rev. B **78**, 045415 (2008).
- [40] K. Kajita, Y. Nishio, N. Tajima, Y. Suzumura, and A. Kobayashi, J. Phys. Soc. Jpn. **83**, 072002 (2014).
- [41] H. Seo, J. Phys. Soc. Jpn. **69**, 805 (2000).
- [42] T. Takahashi, Synth. Met. **133-134**, 261 (2003).
- [43] T. Kakiuchi, Y. Wakabayashi, H. Sawa, T. Takahashi, and T. Nakamura, J. Phys. Soc. Jpn. **76**, 113702 (2007).
- [44] K. Ishikawa, M. Hirata, D. Liu, K. Miyagawa, M. Tamura, and K. Kanoda, Phys. Rev. B **94**, 085154 (2016).
- [45] Y. Tanaka and M. Ogata, J. Phys. Soc. Jpn. **85**, 104706 (2016).
- [46] R. Beyer, A. Dengl, T. Peterseim, S. Wackerow, T. Ivek, A. V. Pronin, D. Schweitzer, and M. Dressel, Phys. Rev. B **93**, 195116 (2016).
- [47] D. Liu, K. Ishikawa, R. Takehara, K. Miyagawa, M. Tamura, and K. Kanoda, Phys. Rev. Lett. **116**, 226401 (2016).

- [48] D. Ohki, Y. Omori, and A. Kobayashi, *Phys. Rev. B* **100**, 075206 (2019).
- [49] M. Hirata, K. Ishikawa, K. Miyagawa, M. Tamura, C. Berthier, D. Basko, A. Kobayashi, G. Matsuno, and K. Kanoda, *Nat. Commun.* **7**, 12666 (2016).
- [50] M. Hirata, K. Ishikawa, G. Matsuno, A. Kobayashi, K. Miyagawa, M. Tamura, C. Berthier, and K. Kanoda, *Science* **358**, 1403 (2017).
- [51] A. Kobayashi and Y. Suzumura, *J. Phys. Soc. Jpn.* **82**, 054715 (2013).
- [52] D. Ohki, M. Hirata, T. Tani, K. Kanoda, and A. Kobayashi, *Phys. Rev. Res.* **2**, 033479 (2020).
- [53] M. Hirata, A. Kobayashi, C. Berthier, and K. Kanoda, *Rep. Prog. Phys.* **84**, 036502 (2021).
- [54] A. Burkov, M. D. Hook, and L. Balents, *Phys. Rev. B* **84**, 235126 (2011).
- [55] C. K. Chiu and A. P. Schnyder, *Phys. Rev. B* **90**, 205136 (2014).
- [56] C. Fang, Y. Chen, H. Y. Kee, and L. Fu, *Phys. Rev. B* **92**, 081201 (2015).
- [57] Z. Gao, M. Hua, H. Zhang, and X. Zhang, *Phys. Rev. B* **93**, 205109 (2016).
- [58] P. R. Wallace, *Phys. Rev.* **71**, 622 (1947).
- [59] H. Weng, C. Fang, Z. Fang, B. A. Bernevig, and X. Dai, *Phys. Rev. X* **5**, 011029 (2015).
- [60] Y. Kim, B. J. Wieder, C. L. Kane, and A. M. Rappe, *Phys. Rev. Lett.* **115**, 036806 (2015).
- [61] R. Yu, H. Weng, Z. Fang, X. Dai, and X. Hu, *Phys. Rev. Lett.* **115**, 036807 (2015).
- [62] J. M. Carter, V. V. Shankar, M. A. Zeb, and H. Y. Kee, *Phys. Rev. B* **85**, 115105 (2012).
- [63] A. Yamakage, Y. Yamakawa, Y. Tanaka, and Y. Okamoto, *J. Phys. Soc. Jpn.* **85**, 013708 (2016).
- [64] R. Kato, H. Cui, T. Tsumuraya, T. Miyazaki, and Y. Suzumura, *J. Am. Chem. Soc.* **139**, 1770 (2017).
- [65] R. Kato and Y. Suzumura, *J. Phys. Soc. Jpn.* **86**, 064705 (2017).
- [66] Y. Suzumura, *J. Phys. Soc. Jpn.* **86**, 124710 (2017).
- [67] Y. Suzumura and R. Kato, *Jpn. J. Appl. Phys.* **56**, 05FB02 (2017).
- [68] Y. Suzumura, H. Cui, and R. Kato, *J. Phys. Soc. Jpn.* **87**, 084702 (2018).
- [69] Y. Suzumura and A. Yamakage, *J. Phys. Soc. Jpn.* **87**, 093704 (2018).

- [70] T. Tsumuraya, R. Kato, and Y. Suzumura, *J. Phys. Soc. Jpn.* **87**, 113701 (2018).
- [71] Y. Suzumura, T. Tsumuraya, R. Kato, H. Matsuura, and M. Ogata, *J. Phys. Soc. Jpn.* **88**, 124704 (2019).
- [72] B. Zhou, S. Ishibashi, T. Ishii, T. Sekine, R. Takehara, K. Miyagawa, K. Kanoda, E. Nishibori, and A. Kobayashi, *Chem. Commun.* **55**, 3327 (2019).
- [73] R.Kato and Y.Suzumura, *J. Phys. Soc. Jpn.* **89**, 044713 (2020).
- [74] T. Kawamura, D. Ohki, B. Zhou, A. Kobayashi, and A. Kobayashi, *J. Phys. Soc. Jpn.* **89**, 074704 (2020).
- [75] T. Kawamura, B. Zhou, A. Kobayashi, and A. Kobayashi, *J. Phys. Soc. Jpn.* **90**, 064710 (2021).
- [76] A. Kobayashi, B. Zhou, R. Takagi, K. Miyagawa, S. Ishibashi, A. Kobayashi, T. Kawamura, E. Nishibori, and K. Kanoda, *Bull. Chem. Soc. Jpn.* **94**, 2540–2562 (2021).
- [77] J. W. Rhim and Y. B. Kim, *Phys. Rev. B* **92**, 045126 (2015).
- [78] A. K. Mitchell and L. Fritz, *Phys. Rev. B* **92**, 121109 (2015).
- [79] S. T. Ramamurthy and T. L. Hughes, *Phys. Rev. B* **95**, 075138 (2017).
- [80] N. H. Shon and T. Ando, *J. Phys. Soc. Jpn.* **67**, 2421 (1998).
- [81] T. Sekine, K. Sunami, T. Hatamura, K. Miyagawa, K. Akimoto, B. Zhou, S. Ishibashi, A. Kobayashi, K. Kanoda, arXiv : 2209.04131
- [82] T. Sekine, T. Hatamura, K. Sunami, K. Miyagawa, and K. Kanoda, *Priv. Commun.*
- [83] H. Seo, S. Ishibashi, Y. Okano, H. Kobayashi, A. Kobayashi, H. Fukuyama, and K. Terakura, *J. Phys. Soc. Jpn.* **77**, 023714 (2008).
- [84] H. Seo, S. Ishibashi, Y. Otsuka, H. Fukuyama, and K. Terakura, *J. Phys. Soc. Jpn.* **82**, 054711 (2013).
- [85] M. Tsuchiizu, Y. Omori, Y. Suzumura, M.-L. Bonnet, V. Robert, S. Ishibashi, and H. Seo, *J. Phys. Soc. Jpn.* **80**, 013703 (2011).
- [86] M. Tsuchiizu, Y. Omori, Y. Suzumura, M.-L. Bonnet, and V. Robert, *J. Chem. Phys.* **136**, 044519 (2012).
- [87] D. Tahara and M. Imada, *J. Phys. Soc. Jpn.* **77**, 114701 (2008).
- [88] T. Misawa, S. Morita, K. Yoshimi, M. Kawamura, Y. Motoyama, K. Ido, T. Ohgoe, M. Imada, and T. Kato, *Comput. Phys. Commun.* **235**, 447 (2019).
- [89] Y. Nakano, Y. Takahashi, K. Ishida, M. Ishikawa, H. Yamochi, and M. Uruichi, *Mater. Chem. Front.* **2**, 752 (2018).

- [90] P. Giannozzi, O. Andreussi, T. Brumme, O. Bunau, M. Buongiorno Nardelli, M. Calandra, R. Car, C. Cavazzoni, D. Ceresoli, M. Cococcioni, N. Colonna, I. Carnimeo, A. Dal Corso, S. de Gironcoli, P. Delugas, R. A. DiStasio Jr., A. Ferretti, A. Floris, G. Fratesi, G. Fugallo, R. Gebauer, U. Gerstmann, F. Giustino, T. Gorni, J. Jia, M. Kawamura, H.-Y. Ko, A. Kokalj, E. Küçükbenli, M. Lazzeri, M. Marsili, N. Marzari, F. Mauri, N. L. Nguyen, H.-V. Nguyen, A. Otero-de-la-Roza, L. Paulatto, S. Poncé, D. Rocca, R. Sabatini, B. Santra, M. Schlipf, A. P. Seitsonen, A. Smogunov, I. Timrov, T. Thonhauser, P. Umari, N. Vast, X. Wu, and S. Baroni, *J. Phys. Condens. Matter* **29**, 465901 (2017).
- [91] D. R. Hamann, *Phys. Rev. B* **88**, 085117 (2013).
- [92] M. Schlipf and F. Gygi, *Comput. Phys. Commun.* **196**, 36-44 (2015).
- [93] J. P. Perdew, K. Burke, and M. Ernzerhof, *Phys. Rev. Lett.* **77**, 3865 (1996).
- [94] K. Nakamura, Y. Yoshimoto, Y. Nomura, T. Tadano, M. Kawamura, T. Kosugi, K. Yoshimi, T. Misawa, and Y. Motoyama, *Comput. Phys. Commun.* **261**, 107781 (2021).
- [95] K. Momma and F. Izumi, VESTA 3 for three-dimensional visualization of crystal, volumetric and morphology data, *J. Appl. Crystallogr.* **44**, 1272 (2011).
- [96] F. Aryasetiawan, M. Imada, A. Georges, G. Kotliar, S. Biermann, and A. I. Lichtenstein, *Phys. Rev. B* **70**, 195104 (2004).
- [97] M. Imada and T. Miyake, *J. Phys. Soc. Jpn.* **79**, 112001 (2010).
- [98] K. Nakamura, Y. Yoshimoto, Y. Nohara, and M. Imada, *J. Phys. Soc. Jpn* **79**, 123708 (2010).
- [99] K. Nakamura, Y. Yoshimoto, and M. Imada, *Phys. Rev. B* **86**, 205117 (2012).
- [100] K. Ido, K. Yoshimi, T. Misawa, and M. Imada, *npj Quantum Mater.* **7**, 48 (2022).
- [101] D. Ohki, K. Yoshimi, A. Kobayashi, and T. Misawa, *Phys. Rev. B* **107**, L041108 (2023).
- [102] K. Yoshimi, T. Misawa, T. Tsumuraya, and H. Seo, *Phys. Rev. Lett.* **131**, 036401 (2023).
- [103] M. C. Gutzwiller, *Phys. Rev. Lett.* **10**, 159 (1963).
- [104] W. F. Brinkman and T. M. Rice, *Phys. Rev. B* **2**, 4302 (1970).
- [105] H. Yokoyama and H. Shiba, *J. Phys. Soc. Jpn.* **56**, 1490 (1987).
- [106] R. Jastrow, *Phys. Rev.* **98**, 1479 (1955).
- [107] M. Capello, F. Becca, M. Fabrizio, S. Sorella, and E. Tosatti, *Phys. Rev. Lett.* **94**, 026406 (2005).

- [108] P. Ring and P. Schuck, *The nuclear many-body problem* (Springer Science & Business Media, 2004).
- [109] T. Mizusaki and M. Imada, *Phys. Rev. B* **69**, 125110 (2004).
- [110] F. Becca and S. Sorella, *Quantum Monte Carlo approaches for correlated systems* (Cambridge University Press, 2017).
- [111] S. Sorella, *Phys. Rev. B* **64**, 024512 (2001).
- [112] I. I. Mazin, *Notes on altermagnetism and superconductivity*, arXiv:2203.05000 .
- [113] S. Katayama, A. Kobayashi, and Y. Suzumura, *Eur. Phys. J. B.* **67**, 139-148 (2009).